Selective Reduction of Aqueous Nitrate to Ammonium with an Electropolymerized Chromium Molecular Catalyst

Maiko J. Askari[1,†], Jeremy D. Kallick[1,†], and Charles C. L. McCrory[1,2,*]

[1]Department of Chemistry, University of Michigan, Ann Arbor, MI, 48109, USA.
[2] Department of Macromolecular Science and Engineering Program, University of Michigan, Ann Arbor, MI, 48109, USA.

† These authors contributed equally to this work.

*Email: cmccrory@umich.edu

ABSTRACT

Nitrate (NO_3^-) is a common nitrogen-containing contaminant in agricultural, industrial, and low-level nuclear wastewater that causes significant environmental damage. In this work, we report a bio-inspired Cr-based molecular catalyst incorporated into a redox polymer that selectively and efficiently reduces aqueous NO_3^- to ammonium (NH_4^+), a desirable value-added fertilizer component and industrial precursor, at rates of ~0.36 mmol NH_4^+ mg_{cat}^{-1} h^{-1} with >90% Faradaic efficiency for NH_4^+. The NO_3^- reduction reaction occurs through a cascade catalysis mechanism involving the stepwise reduction of NO_3^- to NH_4^+ via observed NO_2^- and NH_2OH intermediates. To our knowledge, this is one of the first examples of a molecular catalyst, homogeneous or heterogenized, that is reported to reduce aqueous NO_3^- to NH_4^+ with rates and Faradaic efficiencies comparable to those of state-of-the-art solid-state electrocatalysts. This work highlights a promising and previously unexplored area of electrocatalyst research using polymer-catalyst composites containing complexes with oxophilic transition metal active sites for electrochemical nitrate remediation with nutrient recovery.

INTRODUCTION

The advent of anthropogenic nitrogen species and their agricultural and industrial uses have drastically altered the nitrogen cycle and detrimentally impacted local and global ecosystems.[1-3] NO_x species, and especially NO_3^-, are particularly damaging to marine ecosystems,[4] and are common contaminants found in concentrated streams from nuclear wastewater[5] and industrial processes,[6] or more dilute streams from agricultural runoff.[7] NO_3^- contamination in groundwater results in eutrophication,[8] or "dead zones," in which hypoxic or anoxic conditions result in mass deaths of many pelagic species and the selective overgrowth of those which can survive the harsh conditions.[4,9] Microbial denitrification in contaminated groundwater results in the conversion of NO_x to N_2O, a potent greenhouse gas.[10-12] Furthermore, the US Environmental Protection Agency and the World Health Organization have determined that NO_3^- is a drinking water pollutant, and have established safe drinking water limits of less than 50 $mg_{NO3^-} L^{-1}$.[13] These various detrimental effects of NO_3^- contamination on the environment and human health underscore the need for efficient nitrate remediation technologies.

Existing NO_3^- remediation technologies focus primarily on either separation and concentration of NO_3^- and other NO_x species[14] or bioremediation with nitrate-consuming bacteria.[15,16] The former, while often used for wastewater treatment, results in highly concentrated brines that require further treatment to achieve true remediation.[16] Bioremediation can achieve true remediation, but is hindered by its requirements for a viable bacterial environment, additional chemical substrates (e.g. electron donors), and the risk of pathogenic bacterial growth.[17] A promising alternative strategy is the direct reduction of NO_3^- to other value-added products via the electrochemical NO_3 reduction reaction (NO_3RR).[1,18-20] The electrochemical reduction of NO_3^- to NH_4^+ is particularly desirable as it couples NO_3^- remediation with nutrient recovery.[21,22]

While many solid-state heterogeneous catalysts for nitrate reduction have been developed, molecular electrocatalysts enable improved tuning through synthetic alterations to the active site. Results from these studies can further guide the understanding of mechanism and design principles to produce catalysts with increased activity and selectivity. Although multiple molecular electrocatalysts capable of nitrate reduction to ammonia have been developed, [23-29] complexes containing oxophilic metals including chromium are relatively underexplored, with only one other known example of a Cr-based molecular electrocatalyst.[30] These oxophilic metal complexes are of particular interest because they may be able to reduce NO_3^- via an oxygen atom transfer (OAT) mechanism similar to that observed in nitrate reductase enzymes.[31,32]

In this work, we report a Cr(2,2';6',2"-terpyridine)Cl_3 complex with an appended 2,2':5',2"-terthiophene ($TPTCrCl_3$) that, when electropolymerized onto a glassy carbon electrode (GCE), forms a conductive p-$TPTCrCl_3$ redox polymer film that is active and selective for the electrochemical reduction of NO_3^- to NH_4^+ via a cascade catalysis mechanism. The p-$TPTCrCl_3$ catalyst system is inspired by the nitrate reductase molybdoenzymes that reduce NO_3^- to NO_2^- via an oxo-transfer mechanism from NO_3^- to the Mo-containing active site buried within the enzyme scaffold with controlled substrate and proton transfer.[33-35] Similar to nitrate reductase, our p-$TPTCrCl_3$ system incorporates Cr active sites, with similar oxophilicity as Mo,[36] inside of a polymeric structure that tunes the local microenvironment and controls the transport of substrate and intermediates to enhance reaction selectivity.[37-39] We have previously demonstrated benefits of catalyst microenvironments by encapsulating CO_2 reduction electrocatalysts in polymeric scaffolds.[40,41] Notably, this catalyst system operates in the presence of phosphate, which can cause deactivation of many other heterogenous systems for NO_x reduction due to competitive occupation of available active sites and pore blocking by phosphate.[42-47] The p-$TPTPCrCl_3$ system reduces

NO_3^- to NH_4^+ with fast rates of 0.36 ± 0.01 mmol NH_4^+ mg_{cat}^{-1} h^{-1} with > 90% Faradaic efficiency (FE) for NH_4^+ at only −0.75 V vs RHE. The p-TPTCrCl$_3$ catalyst system represents one of the first examples of a molecular catalyst, homogeneous or heterogenized, that operates with comparable activity and selectivity to state-of-the-art solid-state catalysts for NO_3^- reduction to NH_4^+.

EXPERIMENTAL.

Materials

All purchased chemicals were used as received. Ferrocene carboxylic acid (97%), ferrocene (98%), sodium hydroxide (Anhydrous, BioUltra, ≥ 98%), sodium phosphate monobasic dihydrate (BioUltra, ≥ 99.0%), sodium phosphate dibasic dihydrate (BioUltra, ≥ 99.0%), maleic acid (ReagentPlus, ≥ 99 %), sodium nitrate ($NaNO_3$, 99.999% Trace Metals Basis), sodium nitrite ($NaNO_2$, BioUltra, ≥ 99.0%), phosphoric acid (85% wt in H_2O, 99.99% Trace Metals Basis), sodium carbonate (anhydrous, ACS Reagent, 99.6%), sodium bicarbonate (BioXtra, 99.5-100.5%), potassium carbonate (anhydrous, ACS Reagent, 99+%) isopropanol (ACS Grade, 95%+), potassium hydroxide (ACS Grade, 85%+), tetrakis(triphenylphosphine)palladium(0) (99%), magnesium sulfate (ReagentPlus, ≥ 99.5%), Silver Nitrate (ReagentPlus, ≥ 99.0%), 8-hydroxyquinoline, 5,10,15,20-Tetraphenyl-21H,23H-porphine cobalt(II) (Co(TPP), Dye content 85 %), 1000 ppm Chromium (III) nitrate standard for ICP-MS, and chromium(III) chloride tetrahydrofuran complex (1:3) (97%) were purchased from Millipore-Sigma. Diethyl ether (anhydrous, BHT Stabilized, ACS grade, 99%), petroleum ether (ACS Grade, 36°-86° C BP), dichloromethane (CH_2Cl_2, ACS Grade, 99.5%), tetrahydrofuran (THF, ACS Grade), ethanol (EtOH, ACS Grade, 190 Proof), dimethylsulfoxide (DMSO, ACS Grade, 99.8%), N,N-dimethylformamide (DMF, ACS grade), potassium chloride (KCl, ACS Grade, 99%), potassium

ferricyanide ($K_3Fe(CN)_6$) (99+%), potassium perchlorate ($KClO_4$, ACS Grade), ammonium hydroxide solution (28-30%, ACS Grade), hydrogen peroxide (30%, ACS Grade), Nitric acid (Trace Metal Grade), and sulfuric acid (Optima Grade) were purchased from ThermoFisher Scientific. 1,2-dimethoxyethane (99%), 2,3,5-tribromothiophene (98%), 2-acetylpyridine (99%), and tetrabutylammonium hexafluorophosphate (nBu$_4$PF$_6$, 98%) were purchased from Oakwood Chemical. N-(1-naphthyl)ethylenediamine dihydrochloride (98%+) was purchased from TCI America. 2-thienylboronic acid (97%) and 4-formylphenylboronic acid (97%) were purchased from Matrix Scientific. Sulfanilamide (98%) and hydroxylamine hydrochloride (99%) were purchased from Alfa Aesar.

Argon (Ar, UHP, 99.999%) was purchased from Cryogenic Gases. Nitrogen gas (N_2) was boil-off gas from a liquid nitrogen source. All water used in this study was purified to 18.2 MΩ•cm resistivity in house using a Thermo Scientific GenPure UV-TOC/UF xCAD-plus water purification system. Deuterated Chloroform ($CDCl_3$, 99.8%) and deuterated dimethylsulfoxide (C_2D_6SO, 99.9%) was purchased from Cambridge Isotopic Laboratories. N^{15}-labeled sodium nitrate (≥98 atom % N^{15}, ≥99%), N^{15}-labeled sodium nitrite (≥ 98 atom % N^{15}, ≥ 95%), and N^{15}-labeled hydroxylamine hydrochloride (≥98 atom % N^{15}, ≥95%) were purchased from Millipore Sigma.

Synthetic Procedures

General Instrumentation and Synthetic Procedures. NMR spectra for organic compounds were collected on a Varian MR400 (400 MHz) spectrometer and all chemical shifts are reported in ppm relative to TMS standards. All NMR data analysis was done using MestReNova version 14.1.2 (Mestrelab Research). Elemental analysis was performed by Midwest Microlabs. Some

synthetic steps were carried out under a dry N_2 atmosphere using an mBraun Labstar 4-glove inert atmosphere glovebox.

Synthesis of $TPTCrCl_3$ monomer is summarized in Figure 1, and details for each step are described in detail below.

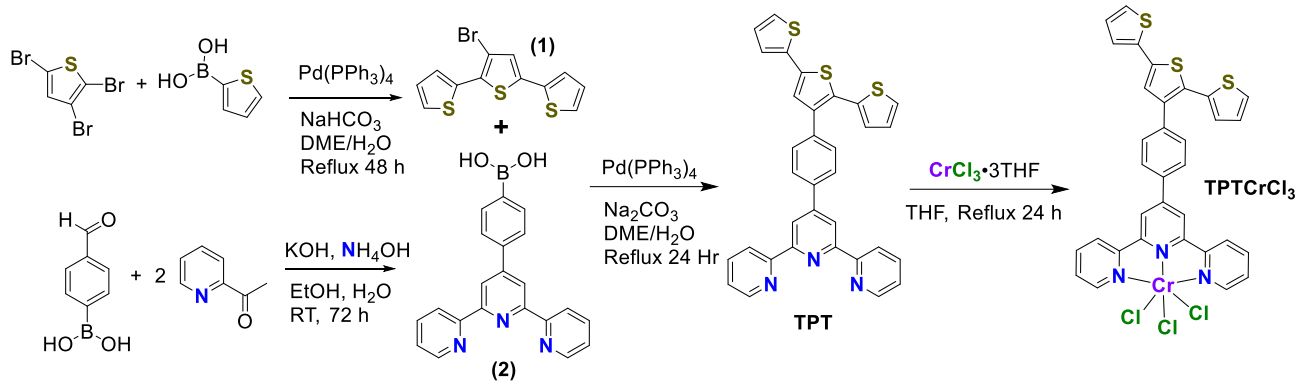

Figure 1. General scheme for the synthesis of the $TPTCrCl_3$ monomer.

3'-bromo-2,2':5',2''-terthiophene (1). 3'-bromo-2,2':5',2''-terthiophene was synthesized based on previously reported methods.[48] A three neck RBF was first charged with 2,3,5-tribromothiophene (0.2 g , 0.623 mmol), 2-thienylboronic acid (0.159 g. 1.240 mmol), 1,2-dimethoxyethane (6 mL), 1 M $NaHCO_3$ solution (2.2 mL), and a stir bar. Then a reflux condenser was added, and the mixture was sparged with nitrogen for 10 minutes. Under constant nitrogen pressure tetrakis-(triphenylphosphine)palladium(0) (0.0416 g , 0.036 mmol) was added and the solution sparged for an additional 5 minutes. The solution was then refluxed overnight. After the first reflux the solution was then cooled to RT and under constant nitrogen pressure additional 2-thienylboronic acid (0.0952 g, 0.744 mmol) and tetrakis-(triphenylphosphine)palladium(0) (0.0416 g , 0.036 mmol) was added and the solution was again refluxed overnight. After disappearance of the 2-thienylboronic acid peak via TLC was confirmed, the reaction was cooled down to RT. The reaction mixture was first filtered, then the 1,2-dimethoxyethane was removed

via reduced pressure. Afterwards, 15 mL of water was added to the residue and it was transferred to a separatory funnel. The product was then extracted 3 times with diethyl ether (30 mL). The combined organic phase was then washed once with a saturated NaCl solution (brine), dried over $MgSO_4$, and filtered. The organic solvent was then removed via reduced pressure to yield a dark brown oil. The crude product was purified via column chromatography on silica gel using petroleum ether/CH_2Cl_2 as the eluent (9:1) to give a yellow oil (95.8 mg, 47% yield) that solidified upon cooling in the freezer at ~5 °C where it was stored. Note that this reaction can be scaled up easily by a factor of 20. **^{1}H NMR** ($CDCl_3$, 400 MHz): δ 7.44 (1H, dd), δ 7.38 (1H, dd), δ 7.29 (1H, dd), δ 7.20 (1H, dd), δ 7.10 (2H, m), δ 7.05 (1H, dd)

(4-([2,2':6',2''-terpyridin]-4'-yl)phenyl)boronic acid (2). A single necked RBF was charged with the following: 100 mL EtOH, 2-acetylpyridine (4.5 mL, 40 mmL), 4-formylphenyl boronic acid (3 g, 20 mmol), and a stir bar. The mixture was then stirred until everything was fully dissolved. Afterwards ammonium hydroxide solution (28%-30%, 58 mL) and KOH (3 g, 55 mmol) was added. The RBF was then capped with a septum and the solution stirred for 72 hours at RT during which an off-white precipitate formed. The resulting precipitate was then collected via vacuum filtration and washed with copious amounts of isopropanol until the run-off was no longer basic. It was then washed with chloroform. The solid was then collected and dried under vacuum to yield 1.5 g (21.23% yield) of an off-white solid. **^{1}H NMR** (CD_3OD, 400 MHz): δ 8.72 (2H, m), δ 8.68 (2H, s), δ 8.66 (2H, d), δ 8.01 (2H, td), δ 7.76 (4H, q). δ 7.49 (2H, qd).

4'-(4-([2,2':5',2''-terthiophen]-3'-yl)phenyl)-2,2':6',2''-terpyridine (TPT). A three-neck RBF was first charged with **(1)** (400 mg, 1.2 mmol), **(2)** (474 mg, 1.34 mmol), 1,2 dimethoxyethane (50 mL), and a stir bar. A reflux condenser was then added and the solution sparged with N_2 for 15 minutes. Separately, K_2CO_3 (500 mg, 36 mmol) was dissolved in minimal

H_2O in a Schlenk tube and sparged with N_2 for 10 minutes. Under constant N_2 pressure tetrakis-(triphenylphosphine)palladium(0) (0.100 g, 0.0865 mmol) was added and the solution sparged for an additional 5 minutes. The K_2CO_3 solution was then added via cannula transfer and the solution refluxed overnight. Progress was checked via TLC and once **(1)** was consumed, the reaction was stopped. After the reaction was completed the 1,2-dimethoxyethane was removed via reduced pressure and the crude residue added to a separatory funnel with additional water (20 mL). The product was then extracted with CH_2Cl_2 (20 mL) three times. The combined organic phases were washed with a saturated NaCl solution (brine), dried over $MgSO_4$, and then the solvent was removed with reduced pressure. The crude material was purified with column chromatography on basic alumina using ethyl acetate/petroleum ether (1:9 to 4:6). The crude material was loaded dry using CH_2Cl_2 to initially load the material on alumina gel. Product was collected as a yellow oil that solidified into yellow crystals (0.345 g, 51.73%). The product was stored in a freezer at ~5 °C until further use. **^{1}H NMR** ($CDCl_3$, 400 MHz): δ 8.78 (2H, s), δ 8.74 (2H, dd), δ 8.69 (2H, d),), δ 7.92 (1H, s), δ 7.91-7.87 (3H, m), δ 7.50-7.56 (2H, m), δ 7.37 (2H, qd), δ 7.20-7.24 (2H, m), δ 7.22 (2H, s), δ 7.06 (1H, q), δ 7.03 (1H, dd), 6.97 (1H, q).

4'-(4-([2,2':5',2''-terthiophen]-3'-yl)phenyl)-2,2':6',2''-terpyridine chromium trichloride (TPTCrCl$_3$). In a nitrogen glovebox a single neck RBF was charged with the TPT ligand (0.0498 g, 0.09 mmol) and a stir bar. In a separate vial, also within the glovebox, chromium(III) chloride tetrahydrofuran complex (1:3) (0.040, 0.109 mmol) was dissolved in THF (10 mL). The THF solution was then transferred to the RBF via pipette which was sealed with a reflux condenser and gas adapter. The reaction set up was then removed from the glovebox, hooked up to a Schlenk line, and refluxed overnight under nitrogen (~24 hr) resulting in the precipitation of a brown solid. The reaction was then cooled, and the precipitate collected via vacuum filtration. The product was

then rinsed with THF and diethyl ether before being dried under vacuum resulting in 25 mg (38.9%) of light brown solid. **Anal. Calcd (found)** $TPTCrCl_3 \cdot 2H_2O$, ($C_{33}H_{25}ON_3S_3CrCl_3$): %C 52.84, (53.29); %H 3.36, (2.94); %N 5.6, (5.71); %S 12.82 (12.95).

Crystal Structure Determination of $TPTCrCl_3$. Green plates of $TPTCrCl_3$ suitable for X-ray diffraction were grown by dissolving a small amount of the compound in CH_3CN in a test tube followed by a thin layer of hexanes as a buffer and a large amount of diethyl ether. A crystal of dimensions 0.02 x 0.02 x 0.01 mm was mounted on a Rigaku AFC10K Saturn 944+ CCD-based X-ray diffractometer equipped with a low temperature device and Micromax-007HF Cu-target micro-focus rotating anode (λ = 1.54187 A) operated at 1.2 kW power (40 kV, 30 mA). The X-ray intensities were measured at 85(1) K with the detector placed at a distance 42.00 mm from the crystal. A total of 2028 images were collected with an oscillation width of 1.0° in ω. The exposure times were 10 s for the low angle images, 60 s for high angle. Rigaku d*trek images were exported to CrysAlisPro for processing and corrected for absorption. The crystal was determined to be a two-component, non-merohedral twin. The domains are related by a 179.98 deg. rotation about the reciprocal (0 0 1) vector. The refined twin fraction was 0.378(2). Reflections from both domains as well as overlaps were used as the basis of a HKLF5 format input file. The integration of the data yielded a total of 40550 reflections to a maximum 2θ value of 140.09° of which 11200 were independent and 8018 were greater than $2\sigma(I)$. The final cell constants (**Table S1**) were based on the xyz centroids of 7501 reflections above $10\sigma(I)$. Analysis of the data showed negligible decay during data collection. The structure was solved and refined with the Bruker SHELXTL (version 2018/3) software package,[49] using the space group P1bar with Z = 2 for the formula $C_{35}H_{26}N_4OS_3Cl_3Cr$. All non-hydrogen atoms were refined anisotropically with the hydrogen atoms placed in idealized positions. Full matrix least-squares refinement based on F^2

converged at R1 = 0.0718 and wR2 = 0.1922 [based on I > 2sigma(I)], R1 = 0.0894 and wR2 = 0.2054 for all data. The supplementary crystallographic data for this paper is attached as a cif file, and also can be found at the Cambridge Crystallographic Data Centre under reference CCDC 2158034.

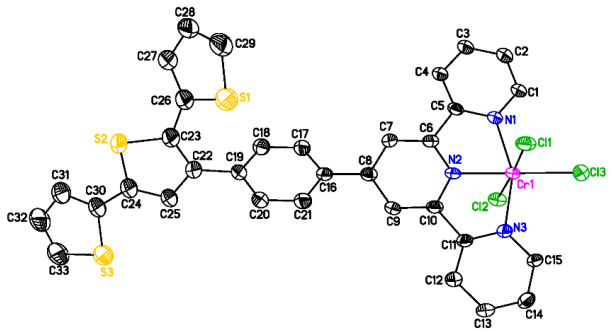

Figure 2. Single crystal structure of the TPTCrCl$_3$ monomer complex, based on single crystals suitable for X-ray analysis grown from acetonitrile/hexanes/diethyl ether. Ellipsoids represent 50% probability. Hydrogen atoms and solvent molecules have been omitted for clarity.

Electrochemical Methods

All electrochemical measurements were conducted using either a Bio-Logic SP-300 or SP-200 potentiostat in a 3-electrode setup, and data were recorded using the Bio-Logic EC-Lab v10.44 software package. Data analysis and figure preparation for the electrochemical studies was performed using Origin 2022 (OriginLab Corporation). All CVs were plotted using IUPAC convention. Before each series of measurements, the uncompensated cell resistance (R_u) was measured with a single-point high frequency impedance measurement. Unless otherwise noted, all electrochemical experiments were conducted at least three times with independently prepared

electrodes and electrolytes, all values reported are the averages of these repetitions, and all reported errors are standard deviations.

General Procedures for Electropolymerization of TPT and TPTCrCl$_3$. Electropolymerization reactions were conducted in a single 50 mL undivided cell. The working electrodes were glassy carbon disk electrodes (GCE) (5 mm diameter, 4 mm thick, 0.196 cm^2 surface area, Sigradur G, HTW Hochtemperatur-Werkstoffe GmbH). The auxiliary electrodes were graphitic carbon rods (99.999%, Strem Chemicals). The reference electrode was a homemade single-junction Ag/AgNO$_3$ (1 mM in MeCN with 0.1 M *n*Bu$_4$NPF$_6$) non-aqueous reference electrode separated from the solution by a CoralPor glass frit (Bioanalytical Systems, Inc.) and externally referenced to the ferrocenium/ferrocene redox couple ($Fc^{+/0}$).

Prior to each electropolymerization experiment, the GCEs were first mechanically polished on silicon carbide abrasive paper (CarbiMet 2, 600/P1200, Buehler) for 30 s. The GCEs were then mounted into a custom-designed brass electrode holder held by a Struers LaboForce-1 specimen mover and polished on a Struers LaboPol-5 polisher. The disks were held by the specimen mover with ~5 psi of applied pressure per disk. The GCEs were polished sequentially on synthetic nap polishing pads (MD Floc, Struers) with alumina abrasive slurries (Struers**)** in an order of 1 μm, 0.3 μm, 0.1 μm, and 0.05 μm for 1 minute each. During polishing, the platen speed was 200 rpm and the head speed was 8 rpm in the opposite rotation from the platen. Between each polishing step, the GCEs and brass electrode holders were rinsed with copious amounts of ultrapure water. After the final polishing step, the glassy carbon disk electrode was sonicated in ultrapure water for ~10 min, then rinsed copious amounts of ultrapure water, and finally dried in an N_2 stream. XPS of the polished GCE show an absence of any elements associated with the p-TPTCrCl$_3$ films (**Figure S1**).

Electropolymerization solutions contained 0.1 M nBu$_4$NPF6 and either saturated (~1 mM) TPTCrCl$_3$ or 1 mM TPT and were mixed on a vortex mixer until the monomer was fully dissolved. Once an electropolymerization solution was prepared, it was used within 24 h and stored in a freezer at ~5 °C when not in use. The reference electrode and auxiliary electrodes were submerged in the electrolyte solution, and the polished working GCE was mounted in an E6 Series internal hardware kit (Pine Research) and suspended in the solution in such a way to minimize distance between the working electrode and the reference electrode, thus minimizing solution resistance. In general, the distance between the working electrode and reference electrode was < 3 cm. The working electrode was held at a constant applied potential of 1.06 V vs $Fc^{+/0}$ (1.20 V vs the Ag/AgNO$_3$ reference) until 20 mC of charge was passed. Immediately afterwards, the working electrode was held at a constant applied potential of −0.140 V vs $Fc^{+/0}$ (0.00 V vs the Ag/AgNO$_3$ reference) for 60 s to discharge the system. The polymer-modified electrode was then removed from the deposition solution, rinsed with dichloromethane, and dried under an N_2 stream (general scheme is shown in **Figure S2**).

The same electropolymerization solution was used for up to 2 depositions within a ~4 h period to minimize changes in the film surface due to precipitates in the deposition solution. Between each electropolymerization reaction, an appropriate amount of dichloromethane was added to the electropolymerization solution to compensate for solvent loss due to evaporation to maintain the constant concentration of the monomer. In addition, between each deposition, the CoralPor glass frit of the reference electrode was gently polished with water on a SiC abrasive paper (CarbiMet 2, 600 grit/P1200). This polishing step was to remove the very top layer of the frit that would clog with intercalated TPTCrCl$_3$ monomer over repeated depositions. In general, CoralPor frits were still replaced every ~12 depositions.

Cyclic Voltammetry (CV) Measurements. Cyclic voltammetry measurements were conducted in an undivided 50 mL electrochemical cell. The working electrode was the polymer-modified GCE mounted into an E6 Series Change-Disk rotating disk electrode (RDE) assembly and affixed to a Pine Research Instrumentation MSR rotator. The auxiliary electrode was a graphitic carbon rod auxiliary electrode (99.999%, Strem Chemicals). The reference electrode and a homemade Ag/AgCl/KCl(sat.) single junction reference electrode separated from the electrolyte by a CoralPor glass frit (Bioanalytical Systems, Inc.) prepared as previously described.[50] The reference electrode was externally referenced to the redox couple of ferrocenecarboxylic acid in in 0.2 M phosphate buffer at pH 7 (0.329 V vs. Ag/AgCl/KCl(sat.)).[51] The electrolyte was a 0.10 M phosphate buffer (0.094 M NaH_2PO_4, 0.006 M Na_2HPO_4) titrated to pH 6 with NaOH. For electrochemical NO_3RR studies, 0.10 M $NaNO_3$ was added to the electrolyte. CVs of variable pH were taken in 0.1 M phosphate buffer titrated to pH 6, 7 and 8 with 0.1 M $NaNO_3$. CVs of variable nitrate concentration were taken in 0.1 M pH 6 phosphate buffer with 0.05, 0.1, 0.2 and 0.4 M $NaNO_3$. CVs of variable buffer concentration were taken in pH 6 phosphate buffer with concentration of 0.05, 0.1, and 0.4 M phosphate with 0.1 M $NaNO_3$. CVs of $NaNO_2$ were taken in 0.1 M pH 6 phosphate buffer with 0.1 M $NaNO_2$. Electrolyte pH was measured using a Fisherbrand Accumet AB200 benchtop pH meter equipped with an Atlas Scientific pH probe electrode. The pH meter was calibrated with a 3-point calibration curve at pH 4.01, 7.00, and 10.01 using Thermo Scientific Orion pH buffer solutions.

All potentials measured against the Ag/AgCl/KCl(sat.) reference were converted to RHE (the real hydrogen electrode) using Equation 1:[52]

$$E_{RHE} = E_{exp} + E_{ref} + 0.059V * pH \qquad (1)$$

E_{RHE} is the potential vs RHE, E_{exp} is the measured potential, E_{ref} is the potential of the reference vs the standard hydrogen electrode (~0.197 V for a Ag/AgCl/KCl(sat.) reference), and $pH = 6$ is the pH of the electrolyte. Before each CV measurement, the electrolyte was sparged with N_2 for a minimum of 10 min, and the solution was blanketed with N_2 during each measurement. Unless otherwise noted, CVs reported were measured with a scan rate of 0.10 V s^{-1} and swept in the negative direction at the start of the scan at 0.55 V vs. RHE. All CVs were *iR* compensated at 85% by the Biologic EC-Lab Software. Typical uncompensated resistance in CV measurements was $R_u \approx 150\ \Omega$.

Estimating Catalyst Loading. The catalyst loading was estimated in three ways. First, loading was determined from the charge passed during the electropolymerization process. Electropolymerization of thiophenes/terthiophene requires a 2-e^- oxidation per monomer (for radical formation), and an additional 0.25 e^- oxidative doping per thiophene subunit.[53,54] Thus, for our terthiophene monomers, each monomer deposited should account for a 2.75 e^- oxidation. The catalyst loading estimated in this manner from our 20 mC deposition is ~1.9×10^{-7} mol cm^{-2} (1.2×10^{17} molecules cm^{-2}, 0.14 mg cm^{-2}). This method of catalyst loading determination does not account for charge lost to formation of soluble oligomers that do not precipitate from solution onto the electrode, and therefore is an overestimation of surface coverage.

In addition, the catalyst loading was calculated using the area under the non-catalytic CVs in 0.10 M phosphate buffer at pH 6. The large reductive redox feature was attributed to two overlapping 1 e^- reduction events associated with the $Cr^{3+/2+}$ and $Cr^{2+/+}$ redox couples. A linear background correction was applied to determine the charge associated with this redox feature (**Figure S3**). Using this method, we estimated a catalyst loading of $6.7 \pm 1.2 \times 10^{-8}$ mol cm^{-2} ($4.4 \pm 0.8 \times 10^{16}$ molecules cm^{-2}, 0.047 ± 0.008 mg cm^{-2}). Due to possible error associated with linear

background correction of non-ideal/sloped CVs, we proceeded with confirming coverage by digestion of catalyst and analysis by ICP-MS.

Finally, the catalyst loading was measured by digesting the deposited p-TPTCrCl$_3$ polymer on the glassy carbon electrode and measuring chromium content in the etching solution by inductively coupled plasma-spectrometry (ICP-MS, PerkinElmer Nexion 2000). p-TPTCrCl$_3$ coated glassy carbon electrodes were placed into a 20 mL scintillation vial with 2 mL of concentrated trace-metal grade HNO_3, sonicated for 10 minutes, and stirred overnight at room temperature.

To confirm that the etching solution sufficiently digested the p-TPTCrCl$_3$ from the surface, the surface composition before-and-after etching was measured using a JEOL JSM-7800FLV Scanning Electron Microscope equipped with an Energy-Dispersive X-ray Spectrometry detector (SEM-EDS). Three independently prepared p-TPTCrCl$_3$ electrodes were investigated using SEM-EDS as deposited, and the same electrodes were then investigated post etching. Composition was determined using point mapping on 5 pattern locations per electrode with 20.0 kV and 9000x magnification. A summary of the elemental composition of before and after etching is shown in **Table S2**, and shows complete loss of N, S, Cr, and Cl during the etching process within the 0.1 weight percent limit of detection of SEM-EDS of bulk materials,[55] consistent with removal of the p-TPTCrCl$_3$ polymer from the surface during the etching process. Note that the as-deposited electrodes also show the presence of P and F in the as-deposited p-TPTCrCl$_3$ electrodes due to residual *n*BuNPF$_6$ electrolyte on the surface from the electrodeposition process.

After the surface etching, the etching solution was then diluted by a factor of 16 with ultrapure water to 1 M HNO_3 concentration, then filtered through a cellulose syringe (0.45μm, Titan 3 regenerated cellulose, Fisher Scientific) and analyzed by ICP-MS. The measured chromium concentration was calibrated against a 5, 10, 20, 30 and 50 ppb solution of chromium (III) nitrate

in 1 M trace-metal grade HNO_3 prepared from a 1000 ppm chromium (III) nitrate ICP-MS standard. The mass and moles of catalyst were estimated from the mass of Cr measured in the ICP-MS as shown in Equations 2-4.

$$\text{mass of Cr (mg)} = \text{x ppb} \times \frac{15.8}{1} \times \frac{\frac{0.001\ \text{mg}}{\text{L}}}{1\ \text{ppb}} \times 0.002\ \text{L} \quad (2)$$

$$\text{mol of Cr} = \text{mass in mg} \times \frac{1\ \text{g}}{1000\ \text{mg}} \times \frac{1\ \text{mol Cr}}{51.99\ \text{g Cr}} \quad (3)$$

$$\text{mass of TPTCrCl}_3\ \text{(mg)} = \text{mol}_{\text{Cr}} \times \frac{1\ \text{mol}_{\text{TPTCrCl3}}}{1\ \text{mol}_{\text{Cr}}} \frac{712.06\ \text{g}}{1\ \text{mol}_{\text{TPTCrCl3}}} \times \frac{1000\ \text{mg}}{1\ \text{g}} \quad (4)$$

The catalyst loading estimated from etching of our 20 mC deposition film is $5.5 \pm 0.7 \times 10^{-8}$ mol $TPTCrCl_3$ cm^{-2} ($3.3 \pm 0.4 \times 10^{16}$ molecules cm^{-2}, 0.039 ± 0.005 mg cm^{-2}).

The catalyst loading determined from all methods demonstrates that the electrodeposited catalyst exists in a multilayer film with 10-100 times the typical loading of a ~ 1.7×10^{-9} mol cm^{-2} (~1.0×10^{15} molecules cm^{-2}) monolayer deposition.[56] The mass-loading activity and turnover frequencies reported in this manuscript were calculated using the coverage determined from ICP-MS.

General Procedure for Drop-casting $TPTCrCl_3$ (Unpolymerized Monomer) on Glassy Carbon Electrode. Glassy carbon electrodes were polished as described above. A 1 mM $TPTCrCl_3$ solution was prepared in N,N-dimethylformamide and coated on the electrodes via dropcasting 6.5 μL of solution, allowing the surface to dry at room temperature, then applying a second coating of 6.5 μL of the solution and drying at room temperature (general scheme shown in **Figure S4**). Coverage was estimated to be ~6.7×10^{-8} mol cm^{-2} using this method.

Controlled Potential Electrolyses. All controlled potential electrolyses were performed in a previously described custom-built H-cell consisting of a sealed main chamber containing the working and reference electrodes and a stir bar and an unsealed auxiliary chamber containing the

auxiliary electrode.[41] The two chambers were separated by a Nafion 117 membrane (Fuel Cell Store). To remove adventitious NH_4^+ from the Nafion membrane, the membrane was pre-treated by 30-min sequential sonication steps in 5% H_2O_2, ultrapure water, 0.5 M H_2SO_4, and again in ultrapure water.[57] The working electrode was a polymer-modified GCE held in an E6 series internal hardware kit (Pine Research Instrumentation) and fitted into a custom PEEK sleeve. The auxiliary electrode was a graphitic carbon rod auxiliary electrode (99.999%, Strem Chemicals). The reference electrode and a homemade Ag/AgCl/KCl(sat.) single junction reference electrode separated from the electrolyte by a CoralPor glass frit (Bioanalytical Systems, Inc.) prepared as previously described.[50] The reference electrode was externally referenced to the redox couple of ferrocenecarboxylic acid in in 0.2 M phosphate buffer at pH 7 (0.329 V vs. Ag/AgCl/KCl(sat.)).[51] The distance between the working electrode and reference electrode was 1 cm and the distance between the working and counter electrodes was 8 cm. The stir bars used were always Fisherbrand Egg-Shaped Bars (19 mm length, 9.5 mm diameter), and the stir plates used were always Thermo Scientific RT Touch Series Magnetic Stirrers (4 L capacity, 30-2000 RPM). CPE measurements were not compensated for uncompensated resistance, and the potential value reported is the real applied potential. In general, the cells used for CPE experiments had $R_u \approx 100\ \Omega$. Note that the cells used the CPE experiments for the reduction of $^{15}NH_2OH$ had a slightly higher $R_u \approx 125\ \Omega$ due to the slightly lower ionic strength in these solutions compared to those containing $Na^{15}NO_3$ and $Na^{15}NO_2$. Only ^{15}N-labeled reactants ($^{15}NO_3^-$, $^{15}NO_2^-$, and $^{15}NH_2OH$) were used in CPE measurements to ensure that any NH_4^+ detected was from the reduction of the ^{15}N-labeled reactants. In general, all CPEs experiments were conducted for 2 h except for CPEs measuring $^{15}NH_2OH$ reduction which were conducted for only 1 h to minimize thermal NH_2OH decomposition.[58]

Prior to each CPE experiment, the electrolyte in the main chamber was sparged with Ar for at least 30 min, and then the main chamber was sealed under a blanket of Ar. After the CPE experiment was complete, a 5-mL aliquot of the headspace was removed with a Pressure-Lok gastight syringe (10 mL, Valco VICI Precision Sampling, Inc.) and analyzed via gas chromatography for any H_2 evolved. Then, a 4-5 mL sample of the electrolyte was removed for the detection of dissolved aqueous products: NO_2^-, NH_2OH, and $^{15}NH_4^+$. The total headspace of the main chamber was then determined by mass balance with water.

Gaseous samples of the headspace were measured using a Thermo Scientific Trace 1310 GC system with two separate analyzer channels for the detection of H_2 and other products. 5-mL headspace aliquots were injected into a 3-mL sample loop, and separated using a custom valve system, column configuration, and method developed by Thermo Fisher Scientific and Custom Solutions Group, LLC. H_2 was detected using an Ar carrier gas and thermal conductivity detector (TCD) calibrated using calibration gas mixtures (SCOTTY Specialty Gas) at H_2 = 0.01%, 0.02%, 0.05%, 0.5%, and 1% v/v. Chromatographs were analyzed using the Chromeleon Console WorkStation software. Faradaic efficiencies (FE) of H_2 were calculated using Equation 5:

$$FE = \frac{\frac{V_{HS}}{V_g} \times G \times n \times F}{Q} \qquad (5)$$

Here, V_{HS} is the headspace volume of the working chamber in mL, V_g is the molar volume of the gas at 25°C and 1.0 atm (24500 mL/mol), G is measured volume percent of H_2 determined by the GC in %, n = 2 is the number of electrons required for H_2 production, F is the Faraday constant in units of C/mol, and Q is the charge passed during the CPE in units of C.

Quantification of dissolved products NO_2^- and NH_2OH was achieved using colorimetric methods described below, and dissolved $^{15}NH_4^+$ was quantified using NMR spectroscopy as

described below. All quantification of liquid products was conducted within ~1.5 h of the completion of the CPE experiment. Faradaic efficiencies (FE) were calculated using Equation 6:

$$FE = \frac{c \times V_{el} \times n \times F}{Q \times MW} \times 100\% \qquad (6)$$

Here, c is the experimentally-determined product concentration in units of g/L, V_{el} is the electrolyte volume in units of L, n is the number of electrons required for the product being quantified (n = 2 for NO_2^-, n = 6 for NH_2OH, n = 8 for $^{15}NH_4^+$), F is the Faraday constant in units of C/mol, Q is charge passed in units of C, and MW is the molar mass of the analyte used in the calibration curve in units of g/mol.

The turnover frequency of the catalyst was calculated by dividing the moles ammonium produced per second by moles of catalyst determined from ICP-MS using Equation 7:

$$TOF = \frac{Q \times FE_{NH4+}}{nF \times t \times mol_{cat}} \qquad (7)$$

Here, Q is the total charge passes in units of Coulombs, FE_{NH4+} is faradaic efficiency for ammonium as a fraction of 1, n is the number of electrons required for ammonium (n = 8 for $^{15}NH_4^+$), t is the time for electrolysis in seconds, F is the Faraday constant in units of C/mol, and mol_{cat} is the moles of catalyst determined by ICP-MS. The error in TOF was determined by error propagation.

Detection of Nitrite, **NO_2^-**. Nitrite was detected using the Greiss reagent,[59,60] which was prepared as follows: 6.0 mL H_3PO_4, 2.0 g of sulfanilamide, and 0.20 g N-(1-naphthyl)ethylenediamine dihydrochloride were dissolved in 100 mL total volume of ultrapure water. The Greiss reagent was stored in the dark and cold in a freezer at ~5 °C for up to 3 weeks. All post-CPE samples were diluted as follows: all samples were diluted 1:10 with 0.1 M pH 6 phosphate buffer *except* samples obtained from CPEs conducted at −0.55 V vs RHE which were diluted 1:2, CPEs conducted on unmetallated TPT-coated electrodes which were diluted 1:4, and

CPEs conducted on bare GCEs and drop-casted $TPTCrCl_3$ which were diluted 1:100. For analysis, a 2.0 mL aliquot of the diluted post-CPE electrolyte sample was combined with 2.0 mL of the Greiss Reagent, briefly shaken, and then stored in the dark for 30 minutes. A UV-Vis spectrum of the resulting solution was collected on a PerkinElmer Lambda 265 UV-Vis Spectrophotometer with fast mode using ultrapure water as the blank. The absorbance at 548 nm was quantified against a calibration curve prepared using different concentrations of $NaNO_2$ in 0.1 M pH 6 phosphate buffer shown in **Figure S5**.

Detection of Hydroxylamine, NH_2OH. Hydroxylamine was detected using the 8-hydroxyquinoline method.[61] This method involves two solutions prepared as follows: Solution A was prepared by dissolving 1.0 g of 8-hydroxyquinoline in EtOH to 100 mL total volume, and Solution B was prepared by dissolving 10.6 g of sodium carbonate in ultrapure water to 100 mL total volume. Solution A was stored in the dark and cold in a freezer at ~5 °C for up to 3 weeks. Solution B did not require special storage procedures and was used for up to 3 weeks. Post-CPE samples were not diluted prior to analysis. For analysis, 1 mL of the post-CPE electrolyte sample was combined with 1 mL of Solution A and mixed briefly. To this solution was then added 1 mL of Solution B. After all solutions were added, the mixture was shaken vigorously by hand to incorporate oxygen into the solution, and then the solution was allowed to sit undisturbed for 60 minutes. A UV-Vis spectrum of the resulting solution was collected on a PerkinElmer Lambda 265 UV-Vis Spectrophotometer with fast mode using ultrapure water as the blank. The absorbance at 700 nm was quantified against a calibration curve prepared using different concentrations of hydroxylamine hydrochloride in 0.1 M pH 6 phosphate buffer shown in **Figure S6**.

A Note on Hydroxylamine Stability. Hydroxylamine solutions are somewhat unstable and thermally decompose to NH_4^+ and other products, and the rate of decomposition increases with

increasing pH.[58] To test hydroxylamine stability under our experimental conditions, we measured the decrease in hydroxylamine concentration following an NO_3^- electrolysis at three different solution pH (**Figure S7**). In phosphate buffer solutions at pH 7, only ~70% of the initial NH_2OH concentration remained after 120 min in the electrolyte solution, whereas in more acidic pH 6 electrolytes, ~94% of the initial NH_2OH concentration remained on this time scale. Based on these results, we used pH 6 phosphate buffers for all of our electrochemical NO_3^- reduction studies to ensure that we could accurately quantify NH_2OH intermediate products with minimal effects of NH_2OH decomposition. In addition, for CPE studies of $^{15}NH_2OH$ reduction, we reduced the CPE time to 60 min to help ensure that the majority of $^{15}NH_4^+$ was from electrochemical reduction and not thermal decomposition, which is minimal at pH 6 over 60 min.

Detection of ^{15}N Ammonium. All N-containing reactants used in CPE studies were ^{15}N-labeled to ensure that all NH_4^+ measured was from the electrochemical reduction of the substrate and not due to adventitious NH_4^+ contamination. $^{15}NH_4^+$ was quantified by adapting a previously reported ^1H-NMR method for rapid $^{15}NH_4^+$ detection.[62] The following solutions were prepared in advance and stored in the dark for up to 2 weeks. Solution A was a 50-µM maleic acid solution in DMSO-d_6 prepared by dissolving 11.6 mg of maleic acid in 50 mL of DMSO, and then diluting a 50-µl aliquot of the resulting solution with 1.950 mL of DMSO-d_6. Solution B was 4.0 M H_2SO_4 in DMSO-d_6 prepared by adding 450 µl of concentrated H_2SO_4 to 1.55 mL of DMSO-d_6. Post-CPE electrolyte samples were not diluted prior to analysis, except for the samples collected after $^{15}NH_2OH$•HCl CPEs which were diluted 1:4 with 100 mM pH 6 phosphate buffer. A sample containing 750 µl of DMSO-d_6, 125 µl of Solution A, 50 µl of Solution B, and a 125 µl aliquot of the post-CPE electrolyte sample was prepared in a scintillation vial, and an aliquot of the sample was introduced into a Bel Bel-Art SP Scienceware 5mm O.D. thin-walled precision NMR tube.

The NMR tube was then capped, shaken vigorously by hand, and briefly sonicated (2-3 s) to remove bubbles formed during the mixing that can interfere with the NMR measurements.

NMR measurements were conducted on a Bruker 600 MHz spectrometer with a Magnex 600/54 active shielded premium magnet with a liquid nitrogen chilled Bruker Prodigy ($^{1}H/^{19}F$)-X broadband probe. ^{1}H-NMR spectra were collected using the lc1pncwps pulse sequence with all parameters unchanged from the default except the interscan delay (d1) which was set to 1.5 s, and the number of scans (ns) that was set to 1024 scans. The larger number of scans used in our measurements as compared to the previously reported method[62] is due to the decreased signal of the liquid nitrogen cooled probe used in this study compared to the helium cooled probe used in the previous report.

All ^{1}H-NMR data was worked up in MestreNova version 14.1.2 (Mestrelab Research). First the spectrum was referenced to the maleic acid peak (6.25 ppm vs TMS). Then, a phase correction was manually applied followed by a baseline correction using the Whittaker Smoother function between 7.4 and 6.1 ppm. The NMR spectral peaks were then integrated as follows: the maleic acid peak between 6.26 and 6.24 ppm, the $^{15}NH_4^+$ peak 1 between 7.130 and 7.095 ppm, and the $^{15}NH_4^+$ peak 2 between 7.245 and 7.210 ppm. The ratio of the ^{15}N peak areas to the maleic acid peak area was compared to a calibration curve to determine the concentration of NH_4^+. The calibration curve was prepared using different concentrations of $^{15}NH_4Cl$ in 0.1 M pH 6 phosphate buffer and can be found in **Figure S8**, along with a representative NMR spectra of $^{15}NH_4Cl$ concentration (**Figure S9**).

***Detection of Nitric Oxide,* NO**. Detection of Nitric Oxide was attempted for CPEs conducted at −0.75 V vs RHE with stir rate of 750 rpm, and at −0.95 V vs RHE at 250 rpm stir rate, using a previously reported method.[63] A 40 μm solution of 5,10,15,20-Tetraphenyl-21H,23H-porphine

cobalt(II) (Co(TPP) in tetrahydrofuran was prepared in a 20 mL vial with a Teflon septum cap in an N_2 filled glove box. A 5 mL gas sample was taken from batch cells following electrolysis and injected into the vial via the septum and shaken to incorporate. A UV-vis was taken on this sample and compared to an equivalently prepared solution of Co(TPP) in THF to look for a shift in the peak at 524 nm.

***Detection of Nitrous Oxide,* $\mathbf{N_2O}$**. Nitrous oxide was detected for electrolysis of $Na^{15}NO_2^-$ by Gas Chromatography Mass Spectrometry (GC-MS). Gaseous samples of the headspace were measured using a Thermo Scientific Trace 1310 GC system equipped with an ISQ 7000 MS detector with a He carrier gas. 5-mL headspace aliquots were injected into a 250uL sample loop with a Carboxen 1010 Plot fused silica capillary column configuration, and method involving an 8 min hold time at 45 ºC and a 14.75 min ramp to 180 ºC. Chromatographs were analyzed using the Chromeleon Console WorkStation software and replotted using Origin 2022 (OriginLab Corporation).

Estimating Mass Transport in H-Cells used in CPEs. To quantify the convective mass transport within the H-cells used in our CPE measurements, we measured the limiting currents for $Fe(CN)_6^{3-}$ reduction at different stir rates. Linear sweep voltammograms (LSVs) were measured using GCE working electrodes mounted into a Pine PEEK shroud assembly, a graphitic rod counter electrode, and an Ag/AgCl/KCl(sat.) single junction reference electrode externally referenced to ferrocenecarboxylic acid as described above. The stir bars and stir plates used were the same as those used for our CPE measurements. The electrolyte was an aqueous solution of 0.010 M $K_3[Fe(CN)_6]$ and 0.1 M $KClO_4$ as supporting electrolyte. LSVs and CVs were measured at scan rate of 50 mV s^{-1}. All LSVs were *iR* compensated at 85% by the Biologic EC-Lab Software. Typical uncompensated resistance within the H-Cell was $R_u < 100\ \Omega$.

Mass transport to the electrode surface within the H-cells was characterized as a function of stir rate using LSVs of $Fe(CN)_6^{3-}$ from −1.5 V to −0.5 V vs Ag/AgCl/KCl(sat.) (**Figure S10**). This potential range is sufficiently negative of the $Fe(CN)_6^{3-/4-}$ couple (0.23 V vs Ag/AgCl/KCl(sat.), **Figure S11),** that we can assume that the currents densities measured in the LSVs are mass-transport limited. The limiting currents were used to calculate the Sherwood numbers, a dimensionless metric of convective mass transport, using Equation 8:[64,65,66]

$$Sh = \frac{k_m r_{el}}{D} \qquad (8)$$

r_{el} = 0.25 cm is the radius of the working electrode, D = 0.65 × 10^{-5} cm^2 s^{-1} is the diffusion coefficient of ferricyanide in 0.1 M aqueous electrolyte,[67] and k_m is the mass-transfer coefficient calculated from Equation 9:[65,68]

$$k_m = \frac{j_{lim}}{nFc}. \qquad (9)$$

j_{lim} is the mass-transport limited current density in units of A cm^{-2}, n = 1 is the number of electrons in the $Fe(CN)_6^{3-/4-}$ reduction process, F is Faraday's constant, and C = 0.01 M is the concentration of ferricyanide. The Sherwood numbers determined in the H-cell as a function of stir rate are shown in **Figure S12**.

For comparison, we also calculated Sherwood numbers for a traditional rotating disk electrode (RDE) setup for $Fe(CN)_6^{3-}$ reduction. The RDE measurements were conducted in an 150 mL cell containing an aqueous solution of 0.010 M $K_3[Fe(CN)_6]$ and 0.1 M $KClO_4$ as supporting electrolyte. The working electrode was a 0.196 cm^2 GCE mounted into an E6 Series Change-Disk RDE assembly and affixed to a Pine Research Instrumentation MSR rotator. The auxiliary electrode was a graphitic carbon rod (99.999%, Strem Chemicals), and the reference electrode was an Ag/AgCl/KCl(sat.) single junction reference electrode. Rotating disk voltammograms (RDEVs) were measured at a scan rate of 0.05 V/s. All RDEVs were *iR* compensated at 85% by

the Biologic EC-Lab Software. Typical uncompensated resistance within the H-Cell was $R_u \approx 60$ Ω. Mass transport to the RDE surface was characterized as a function of rotation rate using RDEVs from −1.5 V to −0.5 V vs Ag/AgCl/KCl(sat.) (**Figure S13**). The resulting mass-transport limited current densities were converted Sherwood numbers as described above are shown in **Figure S12.**

X-Ray Photoelectron Spectroscopy (XPS) Measurements

XPS measurements were conducted using a Kratos Axis Ultra XPS with a monochromatic Al Kα X-ray source operating at 10 mA and 14 kV. All XPS data analysis was done using the CasaXPS version 2.3.17 software package (Casa Software Ltd). Peak positions of the XPS spectra were referenced to the advantageous carbon peak occurring at 284.8 eV. High-resolution spectra were collected with a pass energy of 20 eV and a step size of 0.1 eV. To quantify elemental ratios, peaks in the XPS high-resolution spectra were first fit to symmetric Voight lines shapes comprised of 70% Gaussian and 30% Lorentzian functions with a Shirley background for Nitrogen and Chlorine, and 30% Gaussian and 70% Lorentzian functions with a Shirley background for Chromium and Sulfur. Elemental ratios were calculated by quantifying the total peak area in the N 1s region, the Cr $2p^{3/2}$ peak, the S 2p region, and the Cl 2p region, and then dividing by their respective relative sensitivity factors (as tabulated for the Kratos Ultra XPS instrument).

RESULTS AND DISCUSSION

Synthesis and Characterization of Electropolymerized p-TPTCrCl$_3$ films

The TPTCrCl$_3$ monomer complex was synthesized by first preparing the TPT ligand according to a procedure adapted from previously reported methods,[48] and then metalating with a chromium salt as shown in **Figure 1**. The crystal structure of the TPTCrCl$_3$ monomer is shown in **Figure 2**,

and crystal data and structure refinement in **Table S1.** Full details of the synthetic methods and full characterization data can be found in the experimental section.

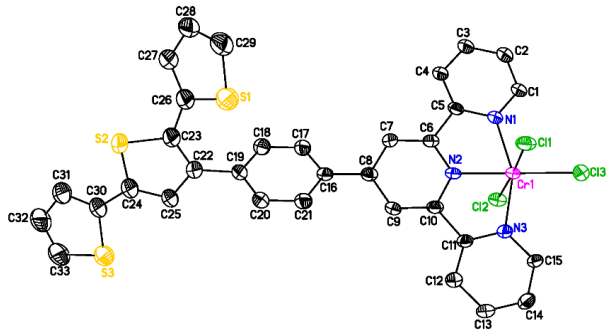

Figure 2. Single crystal structure of the $TPTCrCl_3$ monomer complex, based on single crystals suitable for X-ray analysis grown from acetonitrile/hexanes/diethyl ether. Ellipsoids represent 50% probability. Hydrogen atoms and solvent molecules have been omitted for clarity.

Electropolymerization solutions were 1.0 mM $TPTCrCl_3$ in CH_2Cl_2 with 0.1 M nBu_4NPF_6 supporting electrolyte. Higher concentrations of $TPTCrCl_3$ led to precipitation of the monomer during electropolymerization. Electropolymerization of the $TPTCrCl_3$ monomer was conducted in a single chamber cell in a three-electrode configuration with a 0.196 cm^2 GCE working electrode, a single junction $Ag/AgNO_3$(1.0 mM with 0.1 M $nBuNPF_6$)/MeCN reference electrode, and a carbon rod auxiliary electrode. The GCE working electrode was held at a constant potential of 1.06 V vs $Fc^{+/0}$ until 0.020 C of charge was passed unless otherwise noted (**Figure S14**). Electropolymerization can also be achieved via repeated cyclic voltammograms to oxidizing conditions (**Figure S15**), but the controlled potential method we used results in more reproducible polymer films. Note that electropolymerization was successfully achieved using only CH_2Cl_2 as a solvent, consistent with other studies that show electropolymerization occurs preferentially in CH_2Cl_2 compared to other common solvents.[48,69]

The electropolymerized p-TPTCrCl$_3$ was characterized by X-ray photoelectron spectroscopy (XPS), ICP-MS, and cyclic voltammetry (CV). Representative high-resolution XPS of the N 1s, S 2p, Cr 2p, and Cl 2p regions are shown in **Figure 3**. The ratios of the integrated peaks, corrected for the respective relative sensitivity factors, are shown in **Table S3**. The XPS results closely match the predicted elemental ratios based on the TPTCrCl3 monomer. In particular, the measured N:Cr ratio is 3.23 ± 0.05 compared to a 3:1 predicted ratio, and the measured S:Cr ratio is 2.63 ± 0.12 compared to a 3:1 predicted ratio. The XPS results suggest the deposited film has the same compositional structure as the TPTCrCl$_3$ monomer, which is expected for the p-TPTCrCl$_3$ film. The coverage of the film was determined by etching off a freshly deposited electrode with concentrated nitric acid and measuring chromium content in the post-etch solution by ICP-MS. The full removal of the catalyst via etching was confirmed using SEM-EDS and showed complete loss of Cr, N, S, and Cl within the ~0.1 weight % detection limit after exposure to our etching solution (**Table S2**). The coverage of TPTCrCl$_3$ molecules within the film was determined to be $5.5 \pm 0.7 \times 10^{-8}$ mol cm^{-2} (0.039 ± 0.005 mg cm^{-2}) from ICP-MS analysis of the etching solutions.

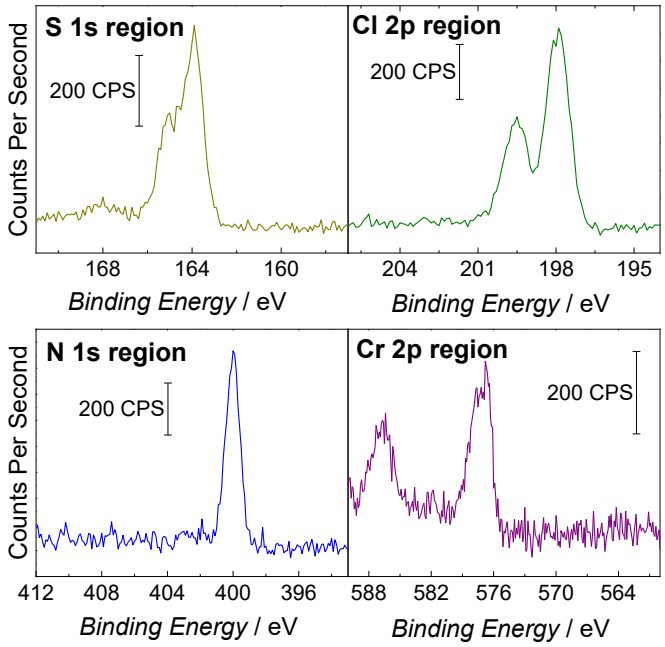

Figure 3. Representative XPS of a p-TPTCrCl$_3$ film formed from a 0.020 C electrodeposition.

Electrocatalytic NO$_3$RR by p-TPTCrCl$_3$ Films

CVs of the p-TPTCrCl$_3$ film were conducted in a three-electrode configuration in a single chamber cell with the p-TPTCrCl$_3$-modified GC working electrode, a single-junction Ag/AgCl/KCl(sat.) aqueous reference electrode, and a carbon rod auxiliary electrode with an N$_2$-saturated 0.1 M pH 6 phosphate buffer as electrolyte. All potentials are referenced to RHE using the procedure described in the experimental section. Representative CVs of the p-TPTCrCl$_3$ film in the presence and absence of 0.1 M NaNO$_3$ are shown in **Figure 4**.

In the absence of NaNO$_3$, a broad, quasireversible redox feature is observed at ~ −0.35 V vs RHE that is attributed to two overlapping 1 e$^-$ events associated with the $Cr^{3+/2+}$ and $Cr^{2+/+}$ redox couples of the TPTCrCl$_3$ units within the film. The coverage of the film was estimated to be 6.7 ± 1.2 × 10^{-8} mol cm^{-2} (0.047 ± 0.008 mg cm^{-2}) based on the charge associated with this redox feature, corrected for background (**Figure S3**), which is in fair agreement with the coverage

obtained by ICP-MS. In the presence of 0.1 M $NaNO_3$, there is a large, irreversible reduction peak at ~−0.56 V vs RHE attributed to the electrocatalytic reduction of NO_3^- by the p-$TPTCrCl_3$ film (**Figure 4**).

We used cyclic voltammetry to study the effects of pH, buffer concentration, and nitrate concentration on catalytic activity for the NO_3RR by p-$TPTCrCl_3$. As the pH is increased from pH 6 to pH 8 in 0.1 M phosphate buffer and with 0.1 M $NaNO_3$, we observe a decrease in the catalytic peak height for the NO_3RR by p-$TPTCrCl_3$ with increasing pH. This result suggests that there may be a kinetic dependence on proton concentration in catalysis (**Figure S16**). However, as we increase the phosphate buffer concentration at pH 6, we observe increased catalytic activity with increasing buffer concentration (**Figure S17**). We attribute this to higher buffering capacity at increased phosphate concentration which moderates local pH swings at the electrode during the catalytic process. Similar effects have been seen in buffer concentration effects of electrochemical CO_2 reduction.[70]

When the nitrate concentration is decreased from 0.1 M to 0.05 M NO_3^- in 0.1 M phosphate buffer at pH 6, we observe a decrease in the catalytic peak current as expected (**Figure S18**). However, if we increase the nitrate concentration to 0.2-0.4 M NO_3^-, we observe a decrease in the catalytic peak at ~−0.56 V vs RHE and the evolution of a new irreversible redox feature at ~−0.75 V vs RHE. This reductive feature at ~−0.75 V vs RHE is consistent with NO_2^- reduction at p-$TPTCrCl_3$ (**Figure S19**). The evolution of this NO_2^- reduction peak at high concentrations of p-$TPTCrCl_3$ suggests that at high NO_3^- concentrations there is a fast initial reduction to NO_2^-, and then further reduction of NO_2^- to more highly reduced products even on the CV timescale.

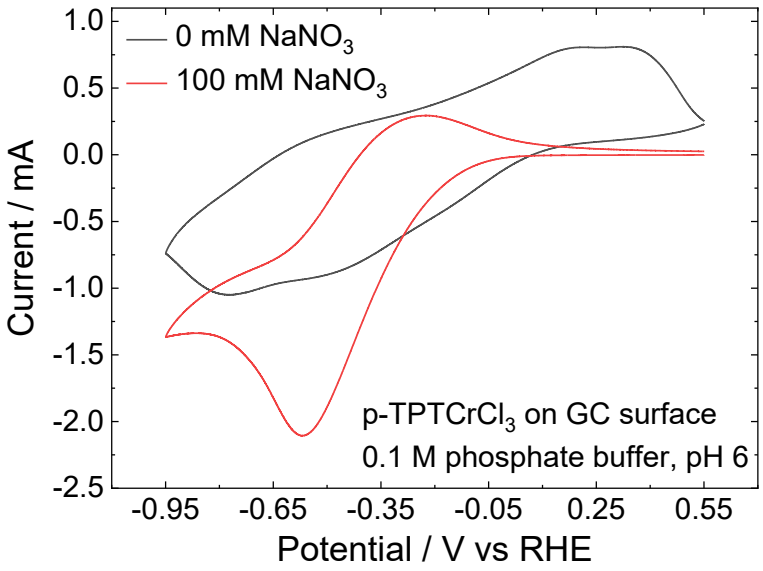

Figure 4. Representative CVs of p-TPTCrCl$_3$ films in 0.10 M phosphate buffer at pH 6 at a scan rate of 0.1 V/s in the absence and presence of 0.1 M NaNO$_3$. The p-TPTCrCl$_3$ film was formed from a 0.020 C electrodeposition.

To quantify further the activity, reaction selectivity, and product distribution for NO_3^- reduction, we conducted a series of 2-h controlled potential electrolysis (CPE) experiments. CPE experiments were conducted in a previously described sealed two-chamber electrochemical cell[41] in which the p-TPTCrCl$_3$-modified GC working electrode and single junction Ag/AgCl/KCl(sat.) reference electrode were located in the first chamber, the carbon rod auxiliary electrode was located in the second chamber, and the two chambers were separated by a Nafion membrane. The first chamber also contained a magnetic Fisherbrand Egg-Shaped Bar, and the stir rate was controlled using a Thermo Scientific RT Touch Series Magnetic Stirrer. All results from the CPE experiments are summarized in **Tables S4-S6.**

Note that we used exclusively isotopically labeled ^{15}N species (e.g. $^{15}NO_3^-$, $^{15}NO_2^-$, and $^{15}NH_2OH$) in our CPE experiments to ensure that any NH_4^+ detected was due solely to substrate reduction and not from adventitious ammonia or catalyst decomposition.[71,72] Electrocatalytically-

generated $^{15}NH_4^+$ product was quantified using a cryo-^{1}H-NMR method in which a specific solvent suppression sequence is combined with pH control of the sample in order to obtain a quantitative ratio between an internal standard (maleic acid) and the proton doublets specific to $^{15}NH_4^+$.[62] Using this cryo-^{1}H-NMR method enabled us to obtain quantitative $^{15}NH_4^+$ data in 40 minutes. Representative NMR spectra from this technique are shown in **Figures S9, S20.** NO_2^-, NH_2OH, and NO were quantified using colorimetric methods,[59-61,63] and H_2 produced from the competitive hydrogen evolution reaction (HER) was quantified using gas chromatography. Calibration curves for the H-NMR and colorimetric methods can be found in **Figures S5-S6, S8**.

For all CPE measurements, the p-TPTCrCl$_3$ films were formed from a 0.020 C electrodeposition. The potential dependence product distribution of NO_3 reduction by p-TPTCrCl$_3$ film in a 0.1 M phosphate buffer at pH 6 and a stir rate of 250 rpm is shown in **Figures 5a-b**. Significant average current density for the NO_3RR in the CPE measurements is observed at potentials more negative than −0.55 V vs. RHE (**Figure 5b**), consistent with onset potential of the NO_3RR observed in the catalytic CVs (**Figure 4**). The highest Faradaic efficiency for NH_4^+ production measured is FE_{NH4} = 86 ± 2, achieved at −0.75 V vs RHE (**Figure 5a**). At potentials more negative than −0.75 V vs RHE, the Faradaic efficiency for NH_4^+ production decreases due to the onset of competitive hydrogen evolution. Importantly, the average partial current density going to NH_4^+ production (j_{NH4}) remains constant, suggesting that the competitive HER does not inhibit the NO_3RR. Small amounts of NO_2^- and NH_2OH were observed at every potential negative of −0.55 V vs. RHE, but these intermediate products accounted for FE < 20%. Attempts to detect NO after CPEs at −0.95 V vs. RHE showed no detectable NO, suggesting that an NO formed is below 0.001 M gas concentration (FE_{NO} < 5 %).[63]

To ensure that the NO_3RR we measured in our experiments was due to the p-$TPTCrCl_3$, we conducted a series of control experiments, the results of which are summarized in **Figure 5c,d** and **Table S7.** First, we measured the NO_3RR activity and selectivity of bare GCEs without p-$TPTCrCl_3$ films. CPEs of these bare GCEs reduced NO_3^- to NO_2^- with high partial current density of j_{NO2} = 3.7 ± 0.6 mA cm^{-2} but produced negligible NH_4^+. We also conducted CPEs with the unmetalated TPT polymer (p-TPT), and the resulting films showed low activity for the NO_3RR of j_{total} < 0.25 mA cm^{-2}, an order-of-magnitude lower than the average current density measured for NO_3RR by p-$TPTCrCl_3$ under otherwise identical conditions. This result suggests that the p-TPT film suppresses any background activity by the GCE, and that Cr incorporation into the film is necessary for NO_3RR activity. Finally, CPEs conducted with p-$TPTCrCl_3$ in the absence of NO_3^- showed low activity of < 0.30 mA cm^{-2} total average current density and no N-containing products. In total, the results of these control experiments confirm that all components of the p-$TPTCrCl_3$ film are necessary for active and selective NO_3RR to NH_4^+. Note that the low total FE reported for the CPEs with unmetalated p-TPT in nitrate solution and p-$TPTCrCl_3$ in nitrate-free solutions is attributed to the very low activity of these systems, resulting in H_2 production near the limit of quantification of our GC instrument (~0.1% v/v) that leads to large inaccuracy in the measured H_2. We also measured the NO_3RR performance of the unpolymerized $TPTCrCl_3$ monomer by drop casting an $TPTCrCl_3$ onto a glassy carbon electrode. The loading of the dropcast unpolymerized $TPTCrCl_3$ was ~6.7 × 10^{-8} mol cm^{-2}, equivalent to the coverage estimation obtained by CVs. Representative CVs of the $TPTCrCl_3$ monomer drop-casted at a coverage of 6.7 × 10^{-8} mol cm^{-2} are shown in **Figure S21.** In the absence of $NaNO_3$, we observe two quasireversible redox features in the CVs at ~ −0.23 V vs RHE and ~ −0.65 V vs RHE that are attributed to the 1 e^- $Cr^{3+/2+}$ and $Cr^{2+/+}$ couples, respectively. We believe these two redox features in the CVs from the dropcast

$TPTCrCl_3$ system in **Figure S21** are analogous to the broad redox features observed in the CV of the p-$TPTCrCl_3$ polymer shown in **Figure 4**. In the presence of 0.1 M $NaNO_3$, the CV of the dropcast $TPTCrCl_3$ monomer shows an irreversible peak attributed to electrocatalytic nitrate reduction, albeit with lower current density compared to the polymerized p-$TPTCrCl_3$ system.

The resulting unpolymerized $TPTCrCl_3$ film reduced NO_3^- to NH_4^+ with FE_{NH4} = 27.2 ± 5% at −0.75 V vs RHE and 250 rpm stir rate (**Figure 5c**), which is much less than the observed FE_{NH4} = 86 ± 2% for the polymerized p-$TPTCrCl_3$ film under identical conditions (**Figure 5a**). Note that similar selectivity has been reported for electrocatalytic NO_3^- reduction by homogeneous trans-$[Cr(cyclam)Cl_2]^+$ catalysts in aqueous solution.[30] These result suggest that incorporation of $TPTCrCl_3$ into the polymer framework is necessary to achieve high selectivity for NO_3RR to NH_3.

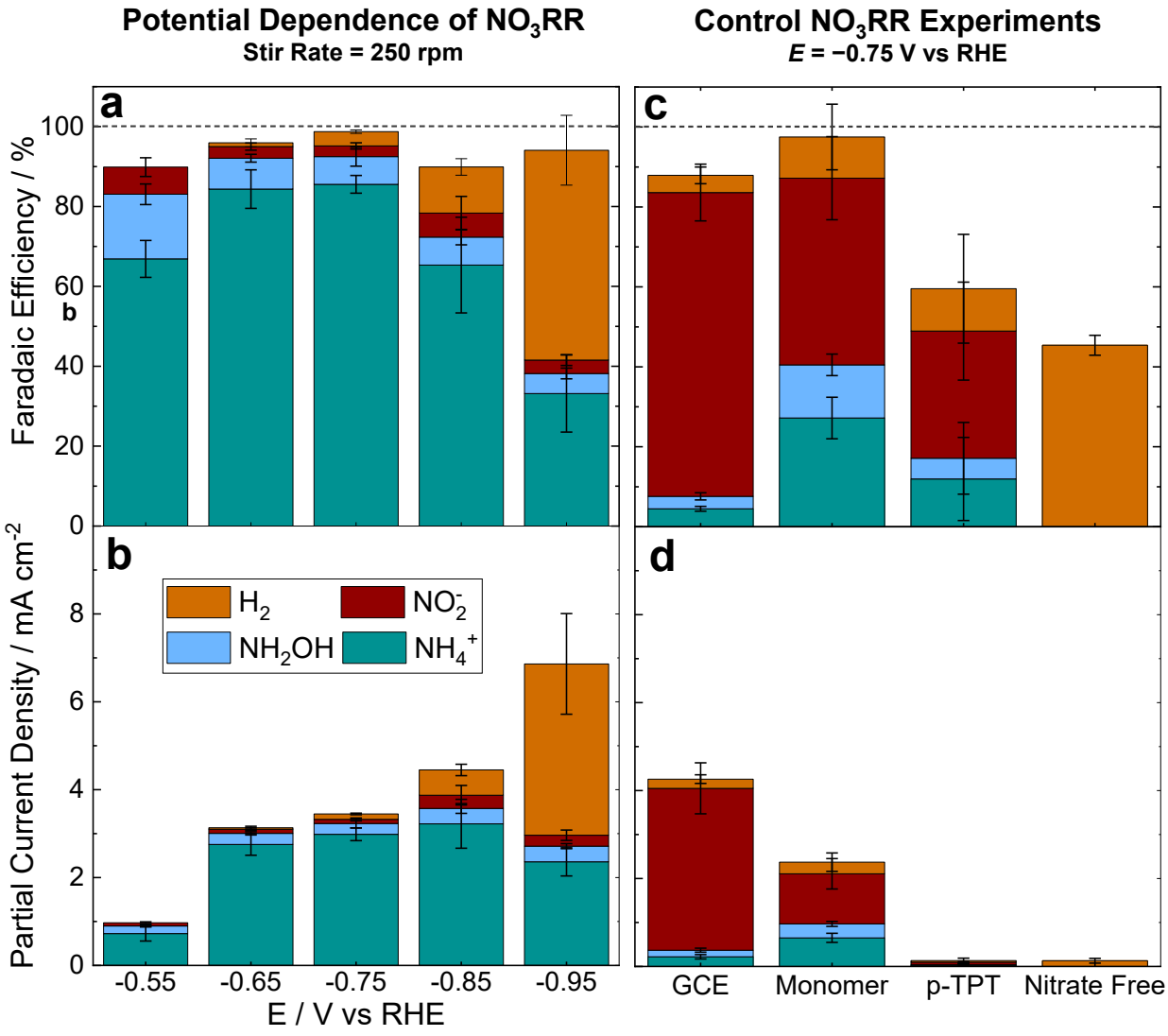

Figure 5. Product distributions from CPE measurements of NO_3RR by p-TPTCrCl$_3$ films formed from a 0.020 C electrodeposition. Unless otherwise noted, all CPEs were conducted in pH 6 phosphate buffer with 0.1 M of ^{15}N-labeled substrate for 2 h. **(a)** Faradaic efficiencies and **(b)** average partial current densities for products of $^{15}NO_3^-$ reduction as a function of applied potential at a stir rate of 250 rpm. **(c)** Faradaic efficiencies and **(d)** average partial current densities products of $^{15}NO_3^-$ reduction control experiments of bare glassy carbon electrode, drop-casted monomer, and polymerized unmetallated ligand and electrolyses of p-TPTCrCl$_3$ in 0.1 M pH 6 phosphate buffer with no added nitrate at a potential of −0.75 V vs RHE and 250 rpm stir rate. All data in these figures are also included in Tables S4 and S7.

Evidence for a Cascade Catalysis Mechanism for NO_3RR by $TPTCrCl_3$

Because we observed small amounts of both NO_2^- and NH_2OH as products in our electrolysis experiments, we hypothesized that the p-$TPTCrCl_3$ system may reduce NO_3^- via a cascade catalysis mechanism, in which NO_3^- is sequentially reduced through various intermediates to the final NH_4^+ product, as has been proposed for another NO_3RR catalyst systems.[73] To test this hypothesis, we first measured the product distribution for the NO_3RR by p-$TPTCrCl_3$ in CPE experiments at different stir rates (**Figure 6a-b**). To make these results cross-comparable with other cell designs, we also determined the Sherwood number, a dimensionless metric of mass transport within the cell, at each stir rate. The Sherwood number was determined from measuring limiting current densities for the reduction of $K_3Fe(CN)_6$ (**Figure S12)** as discussed in the Experimental Section.[66] The Sherwood numbers corresponding to each rotation rate are reported on the top x-axis of **Figure 6a**.

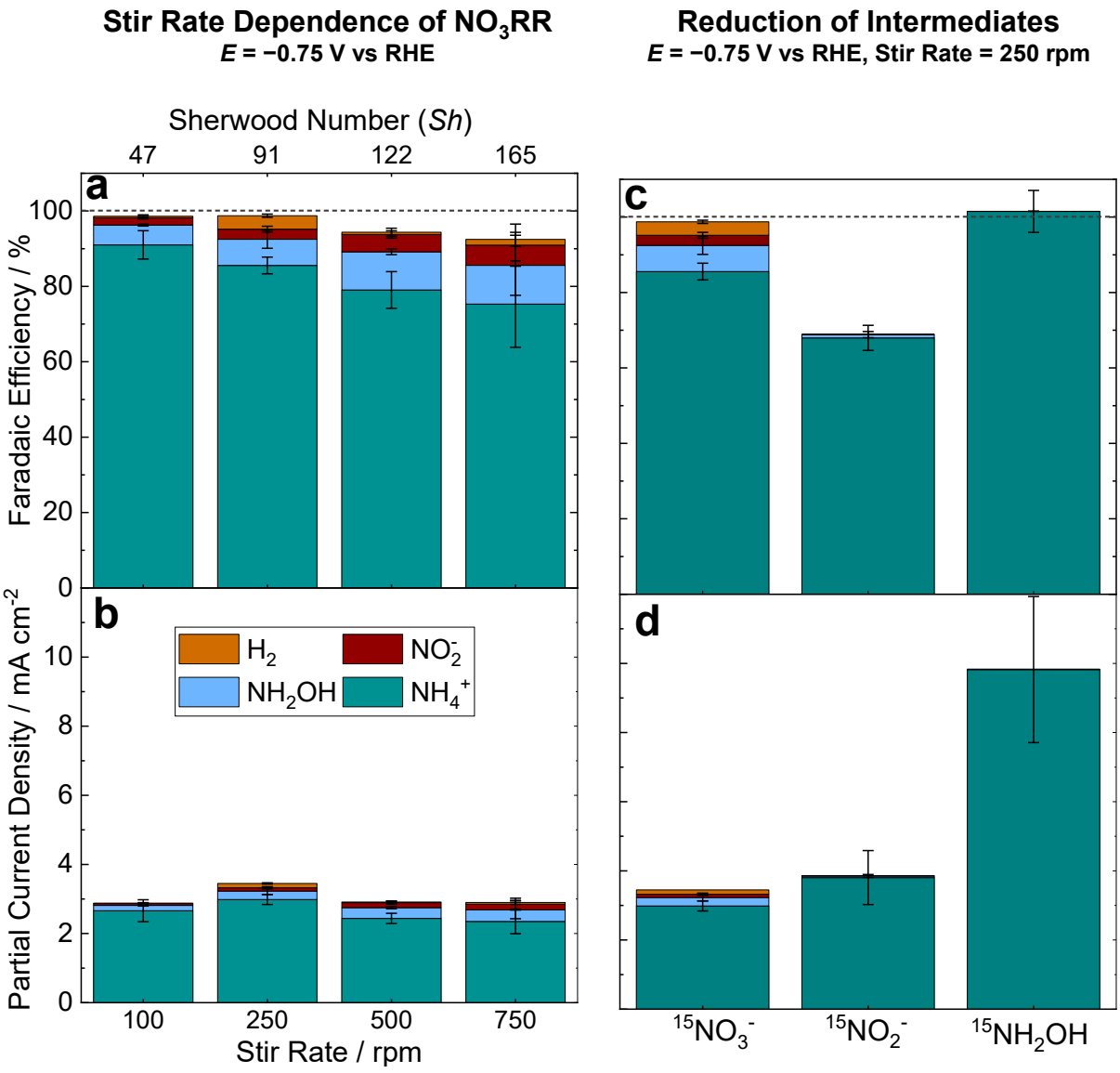

Figure 6. Product distributions from CPE measurements of NO_3RR by p-TPTCrCl$_3$ films formed from a 0.020 C electrodeposition. Unless otherwise noted, all CPEs were conducted in pH 6 phosphate buffer with 0.1 M of ^{15}N-labeled substrate for 2 h. **(a)** Faradaic efficiencies and **(b)** average partial current densities products of $^{15}NO_3^-$ reduction as a function of stir rate at −0.75 V vs RHE. The Sherwood numbers determined at each stir rate are shown in the top x-axis. **(c)** Faradaic efficiencies and **(d)** average partial current densities for products of the reduction of 0.1 M $^{15}NO_3^-$, 0.1 M $^{15}NO_2^-$, and 0.1 M $^{15}NH_2OH$ at −0.75 V vs RHE and a stir rate of 250 rpm. The CPEs for $^{15}NO_3^-$ and $^{15}NO_2^-$ were conducted for 2 h, and the CPEs for NH_2OH were conducted for 1 h. All data in these figures are also included in Tables S5-S6.

We postulated that at slower stir rates, the various reduced intermediates would be retained near the electrode surface and undergo further reduction, resulting in larger observed Faradaic efficiencies for NH_4^+. Conversely, at faster stir rates, we postulated that the reduced intermediates would be swept from the electrode surface, leading to larger Faradaic efficiencies for NO_2^- and NH_2OH. The results shown in **Figure 6a** are consistent with our hypothesis—there is a decrease in Faradaic efficiency for NH_4^+ and increase in Faradaic efficiencies for NO_2^- and NH_2OH as a function of increasing stir rate.

To test further our hypothesis that NO_3RR by p-TPTCrCl$_3$ occurs via a cascade catalysis mechanism, we confirmed that the catalyst film was able to reduce NO_2^- and NH_2OH, the proposed intermediates, to the final NH_4^+ product giving Faradaic efficiencies for NH_4^+ of 68.0 ± 3.3 for reduction of $^{15}NO_2^-$ and 101 ± 5.6 for reduction of $^{15}NH_2OH$. We conducted CPE experiments with 0.1 M $^{15}NO_2^-$ and 0.1 M $^{15}NH_2OH$ at −0.75 V vs RHE and a stir rate of 250 rpm in a pH 6 aqueous phosphate buffer. Note that a shorter 1 hour CPE time was used for reduction of $^{15}NH_2OH$ to limit the extent of its thermal degradation to $^{15}NH_4^+$ and other products under the experimental conditions.[58] We attempted to detect NO after CPEs of $^{15}NO_2^-$ and no NO was detected via the CoTPP method. However, N_2O was detected by GC-MS, showing a fragment with m/z = 46 from $^{15}N_2O$ (**Figure S22-24**). We hypothesize the N_2O is formed from reaction of adsorbed NO or HNO, which builds up in higher concentration during nitrite reduction.[74,75] The resulting product distributions for NO_2^- and NH_2OH reduction are shown in **Figure 6c-d,** along with the NO_3RR results under identical conditions for comparison. The p-TPTCrCl$_3$ film was able to reduce both NO_2^- and NH_2OH to NH_4^+ with high Faradaic efficiency (**Figure 6c**), providing additional support that NO_2^- and NH_2OH are possible intermediates for NO_3RR. Importantly, p-TPTCrCl$_3$ reduces NO_2^- and NH_2OH with higher average current densities than NO_3^-, suggesting that consumption

of these intermediates occurs at faster rates than their production during the NO_3RR. This result is consistent with a cascade catalysis mechanism with a rate-determining NO_3^- activation step.[19]

The p-TPTCrCl_3 system shows continuous activity for NO_3RR during the course of the CPE experiments. However, there is a ~2-fold decrease in measured current during the course of the 2-h CPE (**Figure S25**). In addition, CVs measured of TPTCrCl_3 post-electrolysis also show a change in the voltammetric peaks associated with the p-TPTCrCl_3 after CPE, and a modest decrease in catalytic activity for the NO_3RR (**Figure S26**). Together, these measurements suggest a modest level of catalyst deactivation occurs during the CPE measurements. To investigate the reason for this catalyst deactivation, we conducted postmortem characterization of the catalyst film using XPS and ICP-MS measurements. XPS measurements conducted after the CPE experiments show a complete loss of Cl signal, and an appreciable decrease in the peak heights for Cr, N, and S (**Figure S26**). The loss of Cl in the catalytic cycle during the catalytic cycle is both expected and necessary to open coordination sites on Cr for substrate binding. However, the loss of Cr, N, and S peak intensity in the XPS, coupled with a moderate decrease in the S:Cr ratio from the XPS measurements of the post-CPE p-TPTCrCl_3 films compared to the as-synthesized films (**Table S3**), could indicate modest film degradation or delamination during the CPE experiments. There is also a moderate increase in the N:Cr and N:S ratios by XPS, but interpretation of these results is complicated by the possible incorporation of residual NO_3^- or NH_4^+ in the films post-CPE. However, the Cr coverage measured by ICP-MS following electrolysis was $6.1 \pm 0.4 \times 10^{-8}$ mol cm^{-2}, which is statistically analogous to the coverage = $5.5 \pm 0.7 \times 10^{-8}$ mol cm^{-2} measured for as-synthesized films pre-electrolysis. The ICP-MS results suggest that film delamination is unlikely to be the main reason for the observed loss of catalyst activity, and instead there may be another possible contribution to catalyst deactivation such as increased effective local pH within the film

during the reaction.[76-80] Additional studies are necessary to determine the mechanism of this modest catalyst deactivation, and to determine modifications to the p-TPTCrCl$_3$ system to prevent activity loss.

The catalytic activity of p-TPTCrCl$_3$ for the NO$_3$RR to NH_4^+ is 0.36 ± 0.01 mmol NH_4^+ mg_{cat}^{-1} h^{-1} and a turnover frequency of 0.07 ± 0.01 s^{-1} at −0.75 V vs RHE and 0.33 ± 0.01 mmol NH_4^+ mg_{cat}^{-1} h^{-1} and a turnover frequency of 0.065 ± 0.01 s^{-1} at the more positive −0.65 V vs RHE. For comparison, most other examples of molecular catalysts for aqueous NO_3^- reduction produce less-highly reduced products such as nitrite (NO_2^-) or hydroxylamine (NH_2OH) and/or form NH_4^+ with comparatively low activity and selectivity (**Table S9**).[26-30,73,81-89] One notable exception is a recently developed graphite-conjugated Fe(DIM) macrocycle (GCC-FeDIM) that is reported to reduce NO_3^- to NH_3 with TOF of up to 5.2 s^{-1} at −1.31 V vs SCE in unbuffered 0.5 M Na_2SO_4 at pH 6 (~−0.72 V vs RHE).[25] In addition, Co(cyclam) at Cu electrodes and other coinage metals has been shown to reduce NO_3^- to NH_3 with TOF of up to 0.11 s^{-1} at −1.5 V vs SCE in unbuffered 0.1 M KNO_3 solutions (~−0.86 V vs RHE), although we note that the bare coinage metal electrodes have high background activity for NO$_3$RR even without Co(cyclam),[90-94] and Co(cyclam) shows almost no activity for NO_3^- reduction to NH_3 at Hg electrodes.[26,81] Nonetheless, the p-TPTCrCl$_3$ system is one of the most active molecular catalyst systems reported for selective reduction of aqueous NO_3^- to NH_4^+ with comparable activity and selectivity to recently reported state-of-the-art solid-state catalyst systems (**Figure 7** and **Table S8**). [95-145]

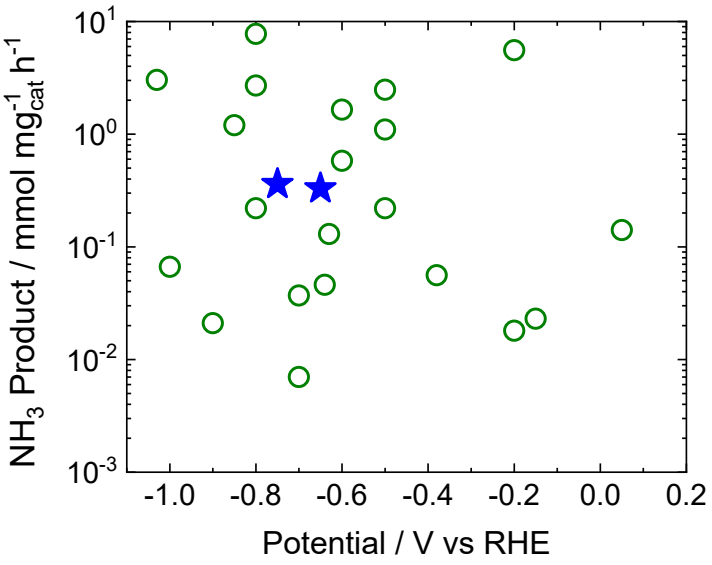

Figure 7. Comparison of the NO_3RR activity to NH_4^+ by p-TPTCrCl$_3$ films from this study (blue stars) to that of selected previously reported solid-state electrocatalysts (green circles). All data from this figure along with relevant citations are included in **Table S8.**

Discussion of Factors Contributing to High NO_3RR Activity and Selectivity by p-TPTCrCl$_3$

When considering the electrochemical NO_3RR by p-TPTCrCl$_3$, we suggest that the high activity, reaction selectivity, and product selectivity for NH_4^+ we observe may be a consequence of three specific factors of the system. First, the oxophilic Cr active sites may activate NO_3^- and other NO_x intermediates via an oxygen atom transfer (OAT) mechanism as illustrated in **Figure 8.** In such a mechanism, the reduced Cr(I) active site first reacts with NO_x to form a Cr(III)-oxide intermediate and a NO_{x-1} species, and the resulting Cr(III)-oxide is reduced back to the Cr(I) active species to restart the cycle. A similar mechanism is reported for Mo-containing nitrate reductase enzymes that selectively reduce NO_3^- to NO_2^-,[31,32] and has been suggested as the operative mechanism for a different homogeneous Cr-based molecular catalyst for NO_3^- reduction.[30] Such an electrochemical OAT mechanism is facilitated by oxophilic metal centers that may not readily

form the metal hydrides necessary for competitive HER, and would lead to the observed increased reaction selectivity for the NO_3RR.

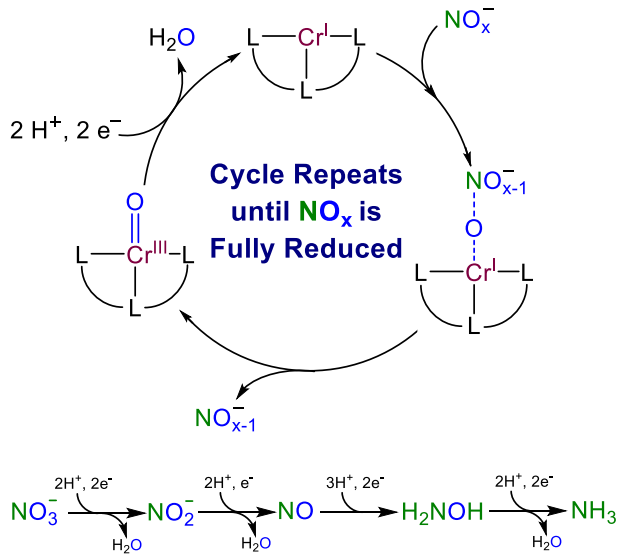

Figure 8. A possible mechanism for the reduction of NO_3^- to NH_3 via sequential electrocatalytic oxygen-atom transfer events.

Second, the oxophilic Cr sites in p-TPTCrCl$_3$ are incorporated within a polymer framework that can help suppress competitive HER by controlling proton delivery to the catalyst sites. This is supported by the control NO_3RR experiments with unmetalated p-TPT which show a large suppression of overall activity, including HER activity, compared to bare GCEs as shown in **Figure 5c-d**. The HER suppression imbued by the p-TPT films is attributed to sluggish proton transport through the polymer film to the GCE electrode.

Third, the polymer framework in p-TPTCrCl$_3$ can help retain NO_x intermediates near the catalyst activity sites, improving selectivity for NH_4^+ over other less reduced products. For example, an unpolymerized dropcasted TPTCrCl$_3$ film shows low product selectivity for NH_4^+

production with FE_{NH4} ~ 30% as shown in **Figure 5c**. For comparison, the polymerized p-TPTCrCl$_3$ shows significantly higher product selectivity for NH_4^+ production with Fe_{NH4} > 85 % under identical electrolyte conditions as shown in **Figure 5a**. We postulate this difference in selectivity is because the polymer framework in p-TPTCrCl$_3$ helps retain released intermediates NO_2^- and NH_2OH near the catalyst sites, thus facilitating their further, stepwise reduction to NH_4^+ as shown in **Figure 8**.

We note that although our NO_3RR results for p-TPTCrCl$_3$ are qualitatively consistent with a sequential oxygen-atom transfer mechanism, they cannot rule out other possible mechanisms for the NO_3RR by this system. Future spectroelectrochemical measurements and electroanalytical studies under more precise hydrodynamic control may help further elucidate the precise mechanism and underlying kinetics of this system.

CONCLUSIONS

We have developed a bio-inspired polymeric Cr catalyst that shows high activity and selectivity for NO_3^- reduction to NH_4^+ with negligible competitive HER. The catalyst likely operates via a cascade catalyst mechanism, in which NO_3^- is sequentially reduced to key intermediates such as NO_2^- and NH_2OH, and finally to NH_4^+. This work shows that early-transition metal molecular catalysts in conductive polymer-catalyst composite films can activate and reduce NO_3^- with competitive activity and selectivity to solid-state catalysts and demonstrates a new paradigm in the development of catalyst-polymer composites with oxophilic metal centers for the activation and reduction of oxyanions. We note that the high activity and selectivity of the p-TPTCrCl$_3$ catalyst was obtained without the extensive systems optimization and engineering

seen in most other reports of active and selective solid-state catalysts for NO_3RR to NH_4^+, suggesting that there is significant room to improve the p-$TPTCrCl_3$ system. Future work with p-$TPTCrCl_3$ and related systems will include studies to elucidate the mechanism of the modest catalyst deactivation and improve stability, and to increase active site exposure and overall activity by electropolymerizing the film onto microstructured and nanostructured supports.

AUTHOR CONTRIBUTIONS

MJA and JDK contributed equally. The manuscript was written through contributions of all authors. All authors have given approval to the final version of the manuscript.

SUPPLEMENTARY INFORMATION

Crystal data and structural refinement for $TPTCrCl_3$ (Supplementary Table S1), X-ray photoelectron spectra of freshly-polished glassy carbon electrode (Supplementary Figure 1), Schematic showing electrodeposition of p-TPTCrCl3 film (Supplementary Figure 2), representative linear background corrections (Supplementary Figure 3), Schematic showing formation of $TPTCrCl_3$ monomer films (Supplementary Figure 4), Elemental composition of p-$TPTCrCl_3$ films before and after etching (Supplementary Table S2), calibration curves for nitrite, and hydroxylamine detection (Supplementary Figures 5-6), representative data illustrating the decomposition of NH_2OH over time in different pH electrolytes (Supplementary Figure 7), calibration curve for ammonium detection (Supplementary Figure 8), representative ^{1}H-NMR spectra of $^{15}NH_4^+$ calibration sample (Supplementary Figure 9), linear sweep voltammogram of ferricyanide reduction in H-cell (Supplementary Figure 10), cyclic voltammogram of ferrocyanide reduction (Supplementary Figure 11), Sherwood number as a function of stir or rotation rate for

ferricyanide reduction (Supplementary Figure 12), linear sweep voltammogram of ferricyanide reduction in RDE cell (Supplementary Figure 13), representative p-TPTCrCl$_3$ depositions (Supplementary Figures 14-15), data table of average elemental ratios from X-ray photoelectron spectroscopy measurements for p-TPTCrCl$_3$ as deposited and after 2-h controlled potential electrolysis (Supplementary Table S3), representative cyclic voltammograms of p-TPTCrCl$_3$ at variable pH in 0.1 M phosphate buffer and 0.1 M $NaNO_3$ (Supplementary Figure 16), representative cyclic voltammograms of p-TPTCrCl$_3$ at variable phosphate buffer concentrations at pH 6 and 0.1 M $NaNO_3$ (Supplementary Figure 17), representative cyclic voltammograms of p-TPTCrCl$_3$ at variable concentrations of $NaNO_3$ in 0.1 M pH 6 phosphate buffer (Supplementary Figure 18), representative cyclic voltammograms of p-TPTCrCl$_3$ with 0.2 and 0.4 M $NaNO_3$ in 0.1 M phosphate buffer overlayed with p-TPTCrCl$_3$ in 0.1 M pH 6 phosphate buffer with 0.1 M $NaNO_2$ (Supplementary Figure 19), data tables of average electrolysis data for p-TPTCrCl$_3$ under different electrolysis conditions (Supplementary Tables S4-S6), representative ^{1}H-NMR spectra of $^{15}NH_4^+$ sample following 2-hour electrolysis (Supplementary Figure 20), data tables of average electrolysis data related to control experiments (Supplementary Table S7), representative cyclic voltammogram of drop-cast TPTCrCl$_3$ (Supplementary Figure 21), Representative gas chromatogram of measured following a 2-hour controlled-potential electrolysis of 100 mM $Na^{15}NO_2$ (Supplementary Figure 22), Representative gas chromatogram of blank run prior to controlled-potential electrolysis of 100 mM $Na^{15}NO_2$ (Supplementary Figure 23), Representative mass spectrum of $^{15}N_2O$ measured by GC-MS following a 2-hour controlled-potential electrolysis (CPE) of 100 mM $Na^{15}NO_2$ (Supplementary Figure 24), representative controlled potential electrolysis measurement (Supplementary Figure 25), representative X-ray photoelectron spectra of p-TPTCrCl$_3$ freshly synthesized and after 2-h controlled potential electrolysis (Supplementary

Figure 26), representative cyclic voltammograms of p-TPTCrCl$_3$ as-synthesized and after 2-h controlled potential electrolysis (Supplementary Figure 27), comparison of the NO_3RR activity and selectivity of p-TPTCrCl$_3$ to state-of-the-art solid state electrocatalysts (Supplementary Table 8), and comparison of the NO_3RR activity and selectivity of p-TPTCrCl$_3$ to molecular electrocatalysts (Supplementary Table 9).

COMPETING INTERESTS

The authors declare no competing interests.

DATA AVAILABILITY

X-ray data are attached as a cif file, and are available free of charge from the Cambridge Crystallographic Data Centre under reference CCDC 2158034. Representative electrochemical measurements, representative X-ray photoelectron spectra, representative cyro-^{1}H-NMR for $^{15}NH_4^+$ quantification, and data tables summarizing electrolysis data are included in the Supplementary information. Raw data are available from the corresponding author on reasonable request.

ACKNOWLEDGEMENTS

This work was supported by an NSF-CAREER grant (CHE-1751791). M. J. A. was partially supported by a PPG Summer Research Fellowship from the Department of Chemistry at the University of Michigan. J. D. K. was partially supported by the National Science Foundation Graduate Research Fellowship Program (DGE 1256260). XPS measurements were conducted at the Michigan Center for Materials Characterization with support from the University of Michigan

College of Engineering and the National Science Foundation (DMR-0420785). SEM-EDS were conducted at the University of Michigan Robert B. Mitchell Electron Microbeam Analysis Lab. Single-crystal X-ray diffraction measurements were conducted with support from the University of Michigan and NSF grant CHE-0840456 for X-ray instrumentation. We thank Dr. Jeff Kampf for crystallographic assistance. ^{1}H-NMR measurements for $^{15}NH_4^+$ quantification reported in this publication were conducted at the University of Michigan BioNMR Core Facility with support from the University of Michigan College of Literature, Sciences and Arts, the Life Sciences Institute, the College of Pharmacy, and the Medical School along with the U-M Biosciences Initiative. We thank Dr. Carlos Morales-Guio for meaningful conversations and suggestions about the hydrodynamics characterization of our system. We thank members of Dr. Nicolai Lehnert's lab including Lizzie Manickas, Michael Lengel, and Jill Harland for suggestions in nitric oxide detection. We thank Dr. Joshua Buss and lab member Andrew Beamer for assistance in N_2O detection via GC-MS.

REFERENCES

(1) van Langevelde, P. H.; Katsounaros, I.; Koper, M. T. M. "Electrocatalytic Nitrate Reduction for Sustainable Ammonia Production," *Joule* **2021**, *5*, 290-294. http://dx.doi.org/10.1016/j.joule.2020.12.025

(2) Mulholland, P. J.; Helton, A. M.; Poole, G. C.; Hall, R. O.; Hamilton, S. K.; Peterson, B. J.; Tank, J. L.; Ashkenas, L. R.; Cooper, L. W.; Dahm, C. N.; Dodds, W. K.; Findlay, S. E. G.; Gregory, S. V.; Grimm, N. B.; Johnson, S. L.; McDowell, W. H.; Meyer, J. L.; Valett, H. M.; Webster, J. R.; Arango, C. P.; Beaulieu, J. J.; Bernot, M. J.; Burgin, A. J.; Crenshaw, C. L.; Johnson, L. T.; Niederlehner, B. R.; O'Brien, J. M.; Potter, J. D.; Sheibley, R. W.; Sobota, D. J.; Thomas, S. M. "Stream denitrification across biomes and its response to anthropogenic nitrate loading," *Nature* **2008**, *452*, 202-205. http://dx.doi.org/10.1038/nature06686

(3) Canfield, D. E.; Glazer, A. N.; Falkowski, P. G. "The Evolution and Future of Earth's Nitrogen Cycle," *Science* **2010**, *330*, 192-196. http://dx.doi.org/10.1126/science.1186120

(4) Diaz, R. J.; Rosenberg, R. "Spreading Dead Zones and Consequences for Marine Ecosystems," *Science* **2008**, *321*, 926-929. http://dx.doi.org/10.1126/science.1156401

(5) Katsounaros, I.; Dortsiou, M.; Kyriacou, G. "Electrochemical reduction of nitrate and nitrite in simulated liquid nuclear wastes," *J. Hazard. Mater.* **2009**, *171*, 323-327. http://dx.doi.org/10.1016/j.jhazmat.2009.06.005

(6) Gu, B.; Chang, J.; Min, Y.; Ge, Y.; Zhu, Q.; Galloway, J. N.; Peng, C. "The role of industrial nitrogen in the global nitrogen biogeochemical cycle," *Scientific Reports* **2013**, *3*, 2579. http://dx.doi.org/10.1038/srep02579

(7) Sebilo, M.; Mayer, B.; Nicolardot, B.; Pinay, G.; Mariotti, A. "Long-term fate of nitrate fertilizer in agricultural soils," *Proc. Natl. Acad. Sci. U.S.A.* **2013**, *110*, 18185-18189. http://dx.doi.org/doi:10.1073/pnas.1305372110

(8) Carpenter, S. R. "Eutrophication of aquatic ecosystems: Bistability and soil phosphorus," *Proc. Natl. Acad. Sci. U.S.A.* **2005**, *102*, 10002-10005. http://dx.doi.org/10.1073/pnas.0503959102

(9) Breitburg, D.; Levin, L. A.; Oschlies, A.; Grégoire, M.; Chavez, F. P.; Conley, D. J.; Garçon, V.; Gilbert, D.; Gutiérrez, D.; Isensee, K.; Jacinto, G. S.; Limburg, K. E.; Montes, I.; Naqvi, S. W. A.; Pitcher, G. C.; Rabalais, N. N.; Roman, M. R.; Rose, K. A.; Seibel, B. A.; Telszewski, M.; Yasuhara, M.; Zhang, J. "Declining oxygen in the global ocean and coastal waters," *Science* **2018**, *359*, eaam7240. http://dx.doi.org/10.1126/science.aam7240

(10) Li, C.; Narayanan, V.; Harriss, R. C. "Model estimates of nitrous oxide emissions from agricultural lands in the United States," *Global Biogeochem. Cycles* **1996**, *10*, 297-306. http://dx.doi.org/10.1029/96GB00470

(11) Beaulieu, J. J.; Tank, J. L.; Hamilton, S. K.; Wollheim, W. M.; Hall, R. O.; Mulholland, P. J.; Peterson, B. J.; Ashkenas, L. R.; Cooper, L. W.; Dahm, C. N.; Dodds, W. K.; Grimm, N. B.; Johnson, S. L.; McDowell, W. H.; Poole, G. C.; Valett, H. M.; Arango, C. P.; Bernot, M. J.; Burgin, A. J.; Crenshaw, C. L.; Helton, A. M.; Johnson, L. T.; O'Brien, J. M.; Potter, J. D.; Sheibley, R. W.; Sobota, D. J.; Thomas, S. M. "Nitrous oxide emission from denitrification in stream and river networks," *Proc. Natl. Acad. Sci. U.S.A.* **2011**, *108*, 214-219. http://dx.doi.org/10.1073/pnas.1011464108

(12) Dore, J. E.; Popp, B. N.; Karl, D. M.; Sansone, F. J. "A large source of atmospheric nitrous oxide from subtropical North Pacific surface waters," *Nature* **1998**, *396*, 63-66. http://dx.doi.org/10.1038/23921

(13) *Guidelines for drinking-water quality: Fourth edition incorporating the first and second addenda*; 4th ed.; World Health Organization, 2022.

(14) Kapoor, A.; Viraraghavan, T. "Nitrate Removal From Drinking Water--Review," *Journal of Environmental Engineering* **1997**, *123*, 371-380. http://dx.doi.org/10.1061/(ASCE)0733-9372(1997)123:4(371)

(15) Mohseni-Bandpi, A.; Elliott, D. J.; Zazouli, M. A. "Biological nitrate removal processes from drinking water supply-a review," *J. Environ. Health Sci. Eng.* **2013**, *11*, 35. http://dx.doi.org/10.1186/2052-336X-11-35

(16) Ghafari, S.; Hasan, M.; Aroua, M. K. "Bio-electrochemical removal of nitrate from water and wastewater—A review," *Bioresour. Technol.* **2008**, *99*, 3965-3974. http://dx.doi.org/10.1016/j.biortech.2007.05.026

(17) Duca, M.; Koper, M. T. M. "Powering denitrification: the perspectives of electrocatalytic nitrate reduction," *Energy Environ. Sci.* **2012**, *5*, 9726-9742. http://dx.doi.org/10.1039/c2ee23062c

(18) Singh, N.; Goldsmith, B. R. "Role of Electrocatalysis in the Remediation of Water Pollutants," *ACS Catal.* **2020**, *10*, 3365-3371. http://dx.doi.org/10.1021/acscatal.9b04167

(19) Garcia-Segura, S.; Lanzarini-Lopes, M.; Hristovski, K.; Westerhoff, P. "Electrocatalytic reduction of nitrate: Fundamentals to full-scale water treatment applications," *Applied Catalysis B: Environmental* **2018**, *236*, 546-568. http://dx.doi.org/https://doi.org/10.1016/j.apcatb.2018.05.041

(20) Wang, Y.; Wang, C.; Li, M.; Yu, Y.; Zhang, B. "Nitrate electroreduction: mechanism insight, in situ characterization, performance evaluation, and challenges," *Chem. Soc. Rev.* **2021**, *50*, 6720-6733. http://dx.doi.org/10.1039/D1CS00116G

(21) Greenlee, L. F. "Recycling fertilizer," *Nat. Energy* **2020**, *5*, 557-558. http://dx.doi.org/10.1038/s41560-020-0670-1

(22) Barrera, L.; Bala Chandran, R. "Harnessing Photoelectrochemistry for Wastewater Nitrate Treatment Coupled with Resource Recovery," *ACS Sustain. Chem. Eng.* **2021**, *9*, 3688-3701. http://dx.doi.org/10.1021/acssuschemeng.0c07935

(23) Taniguchi, I.; Nakashima, N.; Matsushita, K.; Yasukouchi, K. "Electrocatalytic reduction of nitrate and nitrite to hydroxylamine and ammonia using metal cyclams," *Journal of Electroanalytical Chemistry and Interfacial Electrochemistry* **1987**, *224*, 199-209. http://dx.doi.org/http://dx.doi.org/10.1016/0022-0728(87)85092-1

(24) Li, H. L.; Anderson, W. C.; Chambers, J. Q.; Hobbs, D. T. "Electrocatalytic reduction of nitrate in sodium hydroxide solution in the presence of low-valent cobalt-cyclam species," *Inorganic Chemistry* **1989**, *28*, 863-868. http://dx.doi.org/10.1021/ic00304a013

(25) Ghosh, M.; Braley, S. E.; Ezhov, R.; Worster, H.; Valdez-Moreira, J. A.; Losovyj, Y.; Jakubikova, E.; Pushkar, Y. N.; Smith, J. M. "A Spectroscopically Observed Iron Nitrosyl Intermediate in the Reduction of Nitrate by a Surface-Conjugated Electrocatalyst," *Journal of the American Chemical Society* **2022**, *144*, 17824-17831. http://dx.doi.org/10.1021/jacs.2c03487

(26) Taniguchi, I.; Nakashima, N.; Matsushita, K.; Yasukouchi, K. "Electrocatalytic reduction of nitrate and nitrite to hydroxylamine and ammonia using metal cyclams," *J. Electroanal. Chem.* **1987**, *224*, 199-209. http://dx.doi.org/10.1016/0022-0728(87)85092-1

(27) Chebotareva, N.; Nyokong, T. "Metallophthalocyanine catalysed electroreduction of nitrate and nitrite ions in alkaline media," *Journal of Applied Electrochemistry* **1997**, *27*, 975-981. http://dx.doi.org/10.1023/A:1018466021838

(28) Partovi, S.; Xiong, Z.; Kulesa, K. M.; Smith, J. M. "Electrocatalytic Reduction of Nitrogen Oxyanions with a Redox-Active Cobalt Macrocycle Complex," *Inorganic Chemistry* **2022**, *61*, 9034-9039. http://dx.doi.org/10.1021/acs.inorgchem.2c00199

(29) Xu, S.; Ashley, D. C.; Kwon, H.-Y.; Ware, G. R.; Chen, C.-H.; Losovyj, Y.; Gao, X.; Jakubikova, E.; Smith, Jeremy M. "A flexible, redox-active macrocycle enables the electrocatalytic reduction of nitrate to ammonia by a cobalt complex," *Chemical Science* **2018**, *9*, 4950-4958. http://dx.doi.org/10.1039/C8SC00721G

(30) Braley, S. E.; Ashley, D. C.; Jakubikova, E.; Smith, J. M. "Electrode-adsorption activates trans-[Cr(cyclam)Cl2]+ for electrocatalytic nitrate reduction," *Chemical Communications* **2020**, *56*, 603-606. http://dx.doi.org/10.1039/C9CC08550E

(31) Hille, R. "The molybdenum oxotransferases and related enzymes," *Dalton Transactions* **2013**, *42*, 3029-3042. http://dx.doi.org/10.1039/C2DT32376A

(32) Coelho, C.; Romão, M. J. "Structural and mechanistic insights on nitrate reductases," *Protein Science* **2015**, *24*, 1901-1911. http://dx.doi.org/https://doi.org/10.1002/pro.2801

(33) Bertero, M. G.; Rothery, R. A.; Palak, M.; Hou, C.; Lim, D.; Blasco, F.; Weiner, J. H.; Strynadka, N. C. J. "Insights into the respiratory electron transfer pathway from the structure of nitrate reductase A," *Nat. Struct. Mol. Biol.* **2003**, *10*, 681-687. http://dx.doi.org/10.1038/nsb969

(34) Elliott, S. J.; Hoke, K. R.; Heffron, K.; Palak, M.; Rothery, R. A.; Weiner, J. H.; Armstrong, F. A. "Voltammetric Studies of the Catalytic Mechanism of the Respiratory Nitrate Reductase from Escherichia coli: How Nitrate Reduction and Inhibition Depend on the Oxidation State of the Active Site," *Biochemistry* **2004**, *43*, 799-807. http://dx.doi.org/10.1021/bi035869j

(35) Hille, R. "The Mononuclear Molybdenum Enzymes," *Chem. Rev.* **1996**, *96*, 2757-2816. http://dx.doi.org/10.1021/cr950061t

(36) Kepp, K. P. "A Quantitative Scale of Oxophilicity and Thiophilicity," *Inorg. Chem.* **2016**, *55*, 9461-9470. http://dx.doi.org/10.1021/acs.inorgchem.6b01702

(37) Liu, Y.; Leung, K. Y.; Michaud, S. E.; Soucy, T. L.; McCrory, C. C. L. "Controlled Substrate Transport To Electrocatalyst Active Sites For Enhanced Selectivity In The Carbon Dioxide Reduction Reaction," *Comments Inorg. Chem.* **2019**, 1-28. http://dx.doi.org/10.1080/02603594.2019.1628025

(38) Soucy, T. L.; Dean, W. S.; Zhou, J.; Rivera Cruz, K. E.; McCrory, C. C. L. "Considering the Influence of Polymer–Catalyst Interactions on the Chemical Microenvironment of Electrocatalysts for the CO2 Reduction Reaction," *Accounts of Chemical Research* **2022**, *55*, 252-261. http://dx.doi.org/10.1021/acs.accounts.1c00633

(39) Soucy, T. L.; Dean, W. S.; Rivera Cruz, K. E.; Eisenberg, J. B.; Shi, L.; McCrory, C. C. L. "The Influence of pH and Electrolyte Concentration on Fractional Protonation and CO2 Reduction Activity in Polymer-Encapsulated Cobalt Phthalocyanine," *J. Phys. Chem. C* **2023**, *ASAP*. http://dx.doi.org/10.1021/acs.jpcc.3c01490

(40) Kramer, W. W.; McCrory, C. C. L. "Polymer coordination promotes selective CO_2 reduction by cobalt phthalocyanine," *Chem. Sci.* **2016**, *7*, 2506-2515. http://dx.doi.org/10.1039/C5SC04015A

(41) Liu, Y.; McCrory, C. C. L. "Modulating the mechanism of electrocatalytic CO_2 reduction by cobalt phthalocyanine through polymer coordination and encapsulation," *Nat. Commun.* **2019**, *10*, 1683. http://dx.doi.org/10.1038/s41467-019-09626-8

(42) You, Y.; Chang, H.; Zhu, T.; Zhang, T.; Li, X.; Li, J. "The poisoning effects of phosphorus on CeO2-MoO3/TiO2 DeNOx catalysts: NH3-SCR activity and the formation of N2O," *Molecular Catalysis* **2017**, *439*, 15-24. http://dx.doi.org/https://doi.org/10.1016/j.mcat.2017.06.013

(43) Lezcano-Gonzalez, I.; Deka, U.; van der Bij, H. E.; Paalanen, P.; Arstad, B.; Weckhuysen, B. M.; Beale, A. M. "Chemical deactivation of Cu-SSZ-13 ammonia selective catalytic reduction (NH3-SCR) systems," *Applied Catalysis B: Environmental* **2014**, *154-155*, 339-349. http://dx.doi.org/https://doi.org/10.1016/j.apcatb.2014.02.037

(44) Yan, L.; Ji, Y.; Wang, P.; Feng, C.; Han, L.; Li, H.; Yan, T.; Shi, L.; Zhang, D. "Alkali and Phosphorus Resistant Zeolite-like Catalysts for NOx Reduction by NH3," *Environmental Science & Technology* **2020**, *54*, 9132-9141. http://dx.doi.org/10.1021/acs.est.0c03290

(45) Xie, K.; Woo, J.; Bernin, D.; Kumar, A.; Kamasamudram, K.; Olsson, L. "Insights into hydrothermal aging of phosphorus-poisoned Cu-SSZ-13 for NH3-SCR," *Applied Catalysis B: Environmental* **2019**, *241*, 205-216. http://dx.doi.org/https://doi.org/10.1016/j.apcatb.2018.08.082

(46) Li, X.; Li, K.; Peng, Y.; Li, X.; Zhang, Y.; Wang, D.; Chen, J.; Li, J. "Interaction of phosphorus with a FeTiOx catalyst for selective catalytic reduction of NOx with NH3: Influence on surface acidity and SCR mechanism," *Chemical Engineering Journal* **2018**, *347*, 173-183. http://dx.doi.org/https://doi.org/10.1016/j.cej.2018.04.035

(47) Guo, A.; Xie, K.; Lei, H.; Rizzotto, V.; Chen, L.; Fu, M.; Chen, P.; Peng, Y.; Ye, D.; Simon, U. "Inhibition Effect of Phosphorus Poisoning on the Dynamics and Redox of Cu Active Sites in a Cu-SSZ-13 NH3-SCR Catalyst for NOx Reduction," *Environmental Science & Technology* **2021**, *55*, 12619-12629. http://dx.doi.org/10.1021/acs.est.1c03630

(48) Manca, P.; Pilo, M. I.; Casu, G.; Gladiali, S.; Sanna, G.; Scanu, R.; Spano, N.; Zucca, A.; Zanardi, C.; Bagnis, D.; Valentini, L. "A new terpyridine tethered polythiophene: Electrosynthesis and characterization," *J. Polym. Sci., Part A: Polym. Chem.* **2011**, *49*, 3513-3523. http://dx.doi.org/10.1002/pola.24786

(49) Sheldrick, G. "Crystal structure refinement with SHELXL," *Acta Crystallographica Section C* **2015**, *71*, 3-8. http://dx.doi.org/10.1107/S2053229614024218

(50) Leung, K. Y.; McCrory, C. C. L. "Effect and Prevention of Trace Ag^+ Contamination from Ag/AgCl Reference Electrodes on CO_2 Reduction Product Distributions at Polycrystalline Copper Electrodes," *ACS Appl. Energy Mater.* **2019**, *2*, 8283-8293. http://dx.doi.org/10.1021/acsaem.9b01759

(51) Liaudet, E.; Battaglini, F.; Calvo, E. J. "Electrochemical study of sulphonated ferrocenes as redox mediators in enzyme electrodes," *J. Electroanal. Chem.* **1990**, *293*, 55-68. http://dx.doi.org/10.1016/0022-0728(90)80052-8

(52) McCrory, C. C. L.; Jung, S.; Kallick, J. "Chapter 5: Evaluating Electrocatalysts for Solar Water-Splitting Reactions," In *Integrated Solar Fuel Generators*; Sharp, I. D., Atwater, H. A., Lewerenz, H.-J., Eds.; The Royal Society of Chemistry: 2019, p 154-181.

(53) Zotti, G.; Gallazzi, M. C.; Zerbi, G.; Meille, S. V. "Conducting polymers from anodic coupling of some regiochemically defined dialkoxy-substituted thiophene oligomers," *Synth. Met.* **1995**, *73*, 217-225. http://dx.doi.org/10.1016/0379-6779(95)80019-0

(54) Marrec, P.; Fabre, B.; Simonet, J. "Electrochemical and spectroscopic properties of new functionalized polythiophenes electroformed from the oxidation of dithienyls linked by long chain polyether spacers," *J. Electroanal. Chem.* **1997**, *437*, 245-253. http://dx.doi.org/10.1016/S0022-0728(97)00360-4

(55) Goldstein, J. I.; Newbury, D. E.; Michael, J. R.; Ritchie, N. W. M.; Scott, J. H. J.; Joy, D. C.; 4th ed.; Springer New York : Imprint: Springer: New York, NY, 2018, p 1 online resource (XXIII, 550 p. 546 illus., 409 illus. in color.).

(56) Kallick, J. D.; Feng, W.-J.; McCrory, C. C. L. "Controlled Formation of Multilayer Films of Discrete Molecular Catalysts for the Oxygen Reduction Reaction Using a Layer-by-Layer Growth Mechanism Based on Sequential Click Chemistry," *ACS Appl. Energy Mater.* **2020**, *3*, 6222-6231. http://dx.doi.org/10.1021/acsaem.0c00332

(57) Hanifpour, F.; Sveinbjörnsson, A.; Canales, C. P.; Skúlason, E.; Flosadóttir, H. D. "Preparation of Nafion Membranes for Reproducible Ammonia Quantification in Nitrogen Reduction Reaction Experiments," *Angew. Chem. Int. Ed.* **2020**, *59*, 22938-22942. http://dx.doi.org/10.1002/anie.202007998

(58) Wang, Q.; Wei, C.; Pérez, L. M.; Rogers, W. J.; Hall, M. B.; Mannan, M. S. "Thermal Decomposition Pathways of Hydroxylamine: Theoretical Investigation on the Initial Steps," *J. Phys. Chem. A* **2010**, *114*, 9262-9269. http://dx.doi.org/10.1021/jp104144x

(59) Chen, G.-F.; Yuan, Y.; Jiang, H.; Ren, S.-Y.; Ding, L.-X.; Ma, L.; Wu, T.; Lu, J.; Wang, H. "Electrochemical reduction of nitrate to ammonia via direct eight-electron transfer using a copper–molecular solid catalyst," *Nat. Energy* **2020**, *5*, 605-613. http://dx.doi.org/10.1038/s41560-020-0654-1

(60) Schmidt, H. H. H. W.; Kelm, M. "Determination of Nitrate and Nitrite by the Griess Reaction," In *Methods in Nitric Oxide Research*; Feelisch, M., Stamler, J. S., Eds.; John Wiley & Sons: Chichester, 1996, p 491-497.

(61) Arnelle, D. R.; Stamler, J. S. "Detection of Hydroxylamine," In *Methods in Nitric Oxide Research*; Feelisch, M., Stamler, J. S., Eds.; John Wiley & Sons: Chichester, 1996, p 541-552.

(62) Hodgetts, R. Y.; Kiryutin, A. S.; Nichols, P.; Du, H.-L.; Bakker, J. M.; Macfarlane, D. R.; Simonov, A. N. "Refining Universal Procedures for Ammonium Quantification via Rapid 1H NMR Analysis for Dinitrogen Reduction Studies," *ACS Energy Lett.* **2020**, *5*, 736-741. http://dx.doi.org/10.1021/acsenergylett.9b02812

(63) McQuarters, A. B.; Blaesi, E. J.; Kampf, J. W.; Alp, E. E.; Zhao, J.; Hu, M.; Krebs, C.; Lehnert, N. "Synthetic Model Complex of the Key Intermediate in Cytochrome P450 Nitric Oxide Reductase," *Inorganic Chemistry* **2019**, *58*, 1398-1413. http://dx.doi.org/10.1021/acs.inorgchem.8b02947

(64) Clark, E. L.; Resasco, J.; Landers, A.; Lin, J.; Chung, L.-T.; Walton, A.; Hahn, C.; Jaramillo, T. F.; Bell, A. T. "Standards and Protocols for Data Acquisition and Reporting for Studies of the Electrochemical Reduction of Carbon Dioxide," *ACS Catalysis* **2018**, *8*, 6560-6570. http://dx.doi.org/10.1021/acscatal.8b01340

(65) Eisenberg, M.; Tobias, C. W.; Wilke, C. R. "Ionic Mass Transfer and Concentration Polarization at Rotating Electrodes," *Journal of The Electrochemical Society* **1954**, *101*, 306. http://dx.doi.org/10.1149/1.2781252

(66) Jang, J.; Rüscher, M.; Winzely, M.; Morales-Guio, C. G. "Gastight rotating cylinder electrode: Toward decoupling mass transport and intrinsic kinetics in electrocatalysis," *AIChE Journal* **2022**, *68*, e17605. http://dx.doi.org/https://doi.org/10.1002/aic.17605

(67) Jung, S.; Kortlever, R.; Jones, R. J. R.; Lichterman, M. F.; Agapie, T.; McCrory, C. C. L.; Peters, J. C. "Gastight Hydrodynamic Electrochemistry: Design for a Hermetically Sealed Rotating Disk Electrode Cell," *Analytical Chemistry* **2017**, *89*, 581-585. http://dx.doi.org/10.1021/acs.analchem.6b04228

(68) Allen J. Bard, L. R. F. *Electrochemical Methods: Fundamentals and Applications*, 2000.

(69) Manca, P.; Scanu, R.; Zucca, A.; Sanna, G.; Spano, N.; Pilo, M. I. "Electropolymerization of a Ru(II)-terpyridine complex ethynyl-terthiophene functionalized originating different

metallopolymers," *Polymer* **2013**, *54*, 3504-3509. http://dx.doi.org/10.1016/j.polymer.2013.05.026

(70) Kortlever, R.; Shen, J.; Schouten, K. J. P.; Calle-Vallejo, F.; Koper, M. T. M. "Catalysts and Reaction Pathways for the Electrochemical Reduction of Carbon Dioxide," *The Journal of Physical Chemistry Letters* **2015**, *6*, 4073-4082. http://dx.doi.org/10.1021/acs.jpclett.5b01559

(71) Andersen, S. Z.; Čolić, V.; Yang, S.; Schwalbe, J. A.; Nielander, A. C.; McEnaney, J. M.; Enemark-Rasmussen, K.; Baker, J. G.; Singh, A. R.; Rohr, B. A.; Statt, M. J.; Blair, S. J.; Mezzavilla, S.; Kibsgaard, J.; Vesborg, P. C. K.; Cargnello, M.; Bent, S. F.; Jaramillo, T. F.; Stephens, I. E. L.; Nørskov, J. K.; Chorkendorff, I. "A rigorous electrochemical ammonia synthesis protocol with quantitative isotope measurements," *Nature* **2019**, *570*, 504-508. http://dx.doi.org/10.1038/s41586-019-1260-x

(72) Qing, G.; Ghazfar, R.; Jackowski, S. T.; Habibzadeh, F.; Ashtiani, M. M.; Chen, C.-P.; Smith, M. R.; Hamann, T. W. "Recent Advances and Challenges of Electrocatalytic N2 Reduction to Ammonia," *Chem. Rev.* **2020**, *120*, 5437-5516. http://dx.doi.org/10.1021/acs.chemrev.9b00659

(73) Wu, Y.; Jiang, Z.; Lin, Z.; Liang, Y.; Wang, H. "Direct electrosynthesis of methylamine from carbon dioxide and nitrate," *Nature Sustainability* **2021**, *4*, 725-730. http://dx.doi.org/10.1038/s41893-021-00705-7

(74) Rosca, V.; Duca, M.; de Groot, M. T.; Koper, M. T. M. "Nitrogen Cycle Electrocatalysis," *Chemical Reviews* **2009**, *109*, 2209-2244. http://dx.doi.org/10.1021/cr8003696

(75) van der Plas, J. F.; Barendrecht, E. "The electrocatalytic reduction of nitrogen compounds Part I: The electrochemical reduction of nitrite at a rotating platinum ring-disc electrode," *Recueil des Travaux Chimiques des Pays-Bas* **1977**, *96*, 133-136. http://dx.doi.org/https://doi.org/10.1002/recl.19770960505

(76) Zhang, F.; Co, A. C. "Direct Evidence of Local pH Change and the Role of Alkali Cation during CO2 Electroreduction in Aqueous Media," *Angewandte Chemie International Edition* **2020**, *59*, 1674-1681. http://dx.doi.org/https://doi.org/10.1002/anie.201912637

(77) Hall, A. S.; Yoon, Y.; Wuttig, A.; Surendranath, Y. "Mesostructure-Induced Selectivity in CO2 Reduction Catalysis," *Journal of the American Chemical Society* **2015**, *137*, 14834-14837. http://dx.doi.org/10.1021/jacs.5b08259

(78) Liu, X.; Monteiro, M. C. O.; Koper, M. T. M. "Interfacial pH measurements during CO2 reduction on gold using a rotating ring-disk electrode," *Physical Chemistry Chemical Physics* **2023**, *25*, 2897-2906. http://dx.doi.org/10.1039/D2CP05515E

(79) Goyal, A.; Bondue, C. J.; Graf, M.; Koper, M. T. M. "Effect of pore diameter and length on electrochemical CO2 reduction reaction at nanoporous gold catalysts," *Chemical Science* **2022**, *13*, 3288-3298. http://dx.doi.org/10.1039/D1SC05743J

(80) Monteiro, M. C. O.; Mirabal, A.; Jacobse, L.; Doblhoff-Dier, K.; Barton, S. C.; Koper, M. T. M. "Time-Resolved Local pH Measurements during CO2 Reduction Using Scanning Electrochemical Microscopy: Buffering and Tip Effects," *JACS Au* **2021**, *1*, 1915-1924. http://dx.doi.org/10.1021/jacsau.1c00289

(81) Taniguchi, L.; Nakashima, N.; Yasukouchi, K. "Reduction of nitrate to give hydroxylamine at a mercury electrode using cobalt(III)–and nickel(II)–cyclams as catalysts," *Journal of the Chemical Society, Chemical Communications* **1986**, 1814-1815. http://dx.doi.org/10.1039/C39860001814

(82) Kuwabata, S.; Uezumu, S.; Tanaka, K.; Tanaka, T. "Reduction of NO3– giving NH3 using a (Bu4N)3[Mo2Fe6S8(SPh)9]-modified glassy carbon electrode," *Journal of the Chemical Society, Chemical Communications* **1986**, 135-136. http://dx.doi.org/10.1039/C39860000135

(83) Li, H.-L.; Chambers, J. Q.; Hobbs, D. T. "Electrocatalytic reduction of nitrate and nitrite at nafion R-coated electrodes in concentrated sodium hydroxide solution," *Journal of Electroanalytical Chemistry and Interfacial Electrochemistry* **1988**, *256*, 447-453. http://dx.doi.org/https://doi.org/10.1016/0022-0728(88)87018-9

(84) Li, H. L.; Chambers, J. Q.; Hobbs, D. T. "Electroreduction of nitrate ions in concentrated sodium hydroxide solutions at lead, zinc, nickel and phthalocyanine-modified electrodes," *Journal of Applied Electrochemistry* **1988**, *18*, 454-458. http://dx.doi.org/10.1007/BF01093762

(85) Simon, E.; Sablé, E.; Handel, H.; L'Her, M. "Electrodes modified by conducting polymers bearing redox sites: Ni- and Co-cyclam complexes on polypyrrole," *Electrochim. Acta* **1999**, *45*, 855-863. http://dx.doi.org/10.1016/S0013-4686(99)00292-3

(86) Fu, L.-Z.; Zhou, L.-L.; Zhan, S.-Z. "A molecular cobalt catalyst supported by an amine-bis(phenolate) ligand for both electrolytic and photolytic water reduction," *RSC Advances* **2015**, *5*, 84770-84775. http://dx.doi.org/10.1039/C5RA14753K

(87) Shen, J.; Birdja, Y. Y.; Koper, M. T. M. "Electrocatalytic Nitrate Reduction by a Cobalt Protoporphyrin Immobilized on a Pyrolytic Graphite Electrode," *Langmuir* **2015**, *31*, 8495-8501. http://dx.doi.org/10.1021/acs.langmuir.5b00977

(88) Ford, C. L.; Park, Y. J.; Matson, E. M.; Gordon, Z.; Fout, A. R. "A bioinspired iron catalyst for nitrate and perchlorate reduction," *Science* **2016**, *354*, 741-743. http://dx.doi.org/10.1126/science.aah6886

(89) Schachner, J. A.; Wiedemaier, F.; Zwettler, N.; Peschel, L. M.; Boese, A. D.; Belaj, F.; Mösch-Zanetti, N. C. "Catalytic reduction of nitrate by an oxidorhenium (V) complex," *J. Catal.* **2021**, *397*, 108-115. http://dx.doi.org/10.1016/j.jcat.2021.03.028

(90) Reyter, D.; Bélanger, D.; Roué, L. "Study of the electroreduction of nitrate on copper in alkaline solution," *Electrochim. Acta* **2008**, *53*, 5977-5984. http://dx.doi.org/https://doi.org/10.1016/j.electacta.2008.03.048

(91) Butcher, D. P.; Gewirth, A. A. "Nitrate reduction pathways on Cu single crystal surfaces: Effect of oxide and Cl−," *Nano Energy* **2016**, *29*, 457-465. http://dx.doi.org/https://doi.org/10.1016/j.nanoen.2016.06.024

(92) Pérez-Gallent, E.; Figueiredo, M. C.; Katsounaros, I.; Koper, M. T. M. "Electrocatalytic reduction of Nitrate on Copper single crystals in acidic and alkaline solutions," *Electrochim. Acta* **2017**, *227*, 77-84. http://dx.doi.org/https://doi.org/10.1016/j.electacta.2016.12.147

(93) Liu, J.-X.; Richards, D.; Singh, N.; Goldsmith, B. R. "Activity and Selectivity Trends in Electrocatalytic Nitrate Reduction on Transition Metals," *ACS Catalysis* **2019**, *9*, 7052-7064. http://dx.doi.org/10.1021/acscatal.9b02179

(94) Barrera, L.; Silcox, R.; Giammalvo, K.; Brower, E.; Isip, E.; Bala Chandran, R. "Combined Effects of Concentration, pH, and Polycrystalline Copper Surfaces on Electrocatalytic Nitrate-to-Ammonia Activity and Selectivity," *ACS Catal.* **2023**, *13*, 4178-4192. http://dx.doi.org/10.1021/acscatal.2c05136

(95) Jia, R.; Wang, Y.; Wang, C.; Ling, Y.; Yu, Y.; Zhang, B. "Boosting Selective Nitrate Electroreduction to Ammonium by Constructing Oxygen Vacancies in TiO2," *ACS Catalysis* **2020**, *10*, 3533-3540. http://dx.doi.org/10.1021/acscatal.9b05260

(96) Yuting Wang, W. Z., Ranran Jia, Yifu Yu, and Bin Zhang "Unveiling the Activity Origin of a Copper-based Electrocatalyst for Selective Nitrate Reduction to Ammonia," *Angewandte Chemie* **2020**, *59*, 5350-5354.

(97) Wang, Y.; Xu, A.; Wang, Z.; Huang, L.; Li, J.; Li, F.; Wicks, J.; Luo, M.; Nam, D.-H.; Tan, C.-S.; Ding, Y.; Wu, J.; Lum, Y.; Dinh, C.-T.; Sinton, D.; Zheng, G.; Sargent, E. H. "Enhanced Nitrate-to-Ammonia Activity on Copper–Nickel Alloys via Tuning of Intermediate Adsorption," *Journal of the American Chemical Society* **2020**, *142*, 5702-5708. http://dx.doi.org/10.1021/jacs.9b13347

(98) McEnaney, J. M.; Blair, S. J.; Nielander, A. C.; Schwalbe, J. A.; Koshy, D. M.; Cargnello, M.; Jaramillo, T. F. "Electrolyte Engineering for Efficient Electrochemical Nitrate Reduction to Ammonia on a Titanium Electrode," *ACS Sustainable Chemistry & Engineering* **2020**, *8*, 2672-2681. http://dx.doi.org/10.1021/acssuschemeng.9b05983

(99) Li, J.; Zhan, G.; Yang, J.; Quan, F.; Mao, C.; Liu, Y.; Wang, B.; Lei, F.; Li, L.; Chan, A. W. M.; Xu, L.; Shi, Y.; Du, Y.; Hao, W.; Wong, P. K.; Wang, J.; Dou, S.-X.; Zhang, L.; Yu, J. C. "Efficient Ammonia Electrosynthesis from Nitrate on Strained Ruthenium Nanoclusters," *Journal of the American Chemical Society* **2020**, *142*, 7036-7046. http://dx.doi.org/10.1021/jacs.0c00418

(100) Wu, Z.-Y.; Karamad, M.; Yong, X.; Huang, Q.; Cullen, D. A.; Zhu, P.; Xia, C.; Xiao, Q.; Shakouri, M.; Chen, F.-Y.; Kim, J. Y.; Xia, Y.; Heck, K.; Hu, Y.; Wong, M. S.; Li, Q.; Gates, I.; Siahrostami, S.; Wang, H. "Electrochemical ammonia synthesis via nitrate reduction on Fe single atom catalyst," *Nature Communications* **2021**, *12*, 2870. http://dx.doi.org/10.1038/s41467-021-23115-x

(101) Kani, N. C.; Gauthier, J. A.; Prajapati, A.; Edgington, J.; Bordawekar, I.; Shields, W.; Shields, M.; Seitz, L. C.; Singh, A. R.; Singh, M. R. "Solar-driven electrochemical synthesis of ammonia using nitrate with 11% solar-to-fuel efficiency at ambient conditions," *Energy & Environmental Science* **2021**, *14*, 6349-6359. http://dx.doi.org/10.1039/D1EE01879E

(102) Jia, Y.; Ji, Y.-G.; Xue, Q.; Li, F.-M.; Zhao, G.-T.; Jin, P.-J.; Li, S.-N.; Chen, Y. "Efficient Nitrate-to-Ammonia Electroreduction at Cobalt Phosphide Nanoshuttles," *ACS Applied Materials & Interfaces* **2021**, *13*, 45521-45527. http://dx.doi.org/10.1021/acsami.1c12512

(103) Choi, J.; Du, H.-L.; Nguyen, C. K.; Suryanto, B. H. R.; Simonov, A. N.; MacFarlane, D. R. "Electroreduction of Nitrates, Nitrites, and Gaseous Nitrogen Oxides: A Potential Source of Ammonia in Dinitrogen Reduction Studies," *ACS Energy Letters* **2020**, *5*, 2095-2097. http://dx.doi.org/10.1021/acsenergylett.0c00924

(104) Fu, X.; Zhao, X.; Hu, X.; He, K.; Yu, Y.; Li, T.; Tu, Q.; Qian, X.; Yue, Q.; Wasielewski, M. R.; Kang, Y. "Alternative route for electrochemical ammonia synthesis by reduction of nitrate

on copper nanosheets," *Applied Materials Today* **2020**, *19*, 100620. http://dx.doi.org/https://doi.org/10.1016/j.apmt.2020.100620

(105) Wang, Y.; Liu, C.; Zhang, B.; Yu, Y. "Self-template synthesis of hierarchically structured Co3O4@NiO bifunctional electrodes for selective nitrate reduction and tetrahydroisoquinolines semi-dehydrogenation," *Science China Materials* **2020**, *63*, 2530-2538. http://dx.doi.org/10.1007/s40843-020-1365-0

(106) Xu, Y.; Wang, M.; Ren, K.; Ren, T.; Liu, M.; Wang, Z.; Li, X.; Wang, L.; Wang, H. "Atomic defects in pothole-rich two-dimensional copper nanoplates triggering enhanced electrocatalytic selective nitrate-to-ammonia transformation," *Journal of Materials Chemistry A* **2021**, *9*, 16411-16417. http://dx.doi.org/10.1039/D1TA04743D

(107) Wang, J.; Cai, C.; Wang, Y.; Yang, X.; Wu, D.; Zhu, Y.; Li, M.; Gu, M.; Shao, M. "Electrocatalytic Reduction of Nitrate to Ammonia on Low-Cost Ultrathin CoOx Nanosheets," *ACS Catalysis* **2021**, *11*, 15135-15140. http://dx.doi.org/10.1021/acscatal.1c03918

(108) Zhao, X.; Hu, G.; Tan, F.; Zhang, S.; Wang, X.; Hu, X.; Kuklin, A. V.; Baryshnikov, G. V.; Ågren, H.; Zhou, X.; Zhang, H. "Copper confined in vesicle-like BCN cavities promotes electrochemical reduction of nitrate to ammonia in water," *Journal of Materials Chemistry A* **2021**, *9*, 23675-23686. http://dx.doi.org/10.1039/D1TA05718A

(109) Lei, F.; Xu, W.; Yu, J.; Li, K.; Xie, J.; Hao, P.; Cui, G.; Tang, B. "Electrochemical synthesis of ammonia by nitrate reduction on indium incorporated in sulfur doped graphene," *Chemical Engineering Journal* **2021**, *426*, 131317. http://dx.doi.org/https://doi.org/10.1016/j.cej.2021.131317

(110) Yao, Q.; Chen, J.; Xiao, S.; Zhang, Y.; Zhou, X. "Selective Electrocatalytic Reduction of Nitrate to Ammonia with Nickel Phosphide," *ACS Applied Materials & Interfaces* **2021**, *13*, 30458-30467. http://dx.doi.org/10.1021/acsami.0c22338

(111) Yin, H.; Chen, Z.; Xiong, S.; Chen, J.; Wang, C.; Wang, R.; Kuwahara, Y.; Luo, J.; Yamashita, H.; Peng, Y.; Li, J. "Alloying effect-induced electron polarization drives nitrate electroreduction to ammonia," *Chem Catalysis* **2021**, *1*, 1088-1103. http://dx.doi.org/https://doi.org/10.1016/j.checat.2021.08.014

(112) Wei, Z.; Niu, X.; Yin, H.; Yu, S.; Li, J. "Synergistic effect of oxygen defects and hetero-phase junctions of TiO2 for selective nitrate electroreduction to ammonia," *Applied Catalysis A: General* **2022**, *636*, 118596. http://dx.doi.org/https://doi.org/10.1016/j.apcata.2022.118596

(113) Xie, L.; Hu, L.; Liu, Q.; Sun, S.; Zhang, L.; Zhao, D.; Liu, Q.; Chen, J.; Li, J.; Ouyang, L.; Alshehri, A. A.; Kong, Q.; Sun, X. "High-performance electrochemical nitrate reduction to ammonia under ambient conditions using NiFe2O4 nanosheet arrays," *Inorganic Chemistry Frontiers* **2022**, *9*, 3392-3397. http://dx.doi.org/10.1039/D2QI00827K

(114) Zhang, R.; Guo, Y.; Zhang, S.; Chen, D.; Zhao, Y.; Huang, Z.; Ma, L.; Li, P.; Yang, Q.; Liang, G.; Zhi, C. "Efficient Ammonia Electrosynthesis and Energy Conversion through a Zn-Nitrate Battery by Iron Doping Engineered Nickel Phosphide Catalyst," *Advanced Energy Materials* **2022**, *12*, 2103872. http://dx.doi.org/https://doi.org/10.1002/aenm.202103872

(115) Zhang, S.; Li, M.; Li, J.; Song, Q.; Liu, X. "High-ammonia selective metal–organic framework–derived Co-doped Fe/Fe2O3 catalysts for electrochemical nitrate reduction," *Proceedings of the National Academy of Sciences* **2022**, *119*, e2115504119. http://dx.doi.org/10.1073/pnas.2115504119

(116) Cai, J.; Qin, S.; Akram, M. A.; Hou, X.; Jin, P.; Wang, F.; Zhu, B.; Li, X.; Feng, L. "In situ reconstruction enhanced dual-site catalysis towards nitrate electroreduction to ammonia," *Journal of Materials Chemistry A* **2022**, *10*, 12669-12678. http://dx.doi.org/10.1039/D2TA01772E

(117) Zhang, N.; Shang, J.; Deng, X.; Cai, L.; Long, R.; Xiong, Y.; Chai, Y. "Governing Interlayer Strain in Bismuth Nanocrystals for Efficient Ammonia Electrosynthesis from Nitrate Reduction," *ACS Nano* **2022**, *16*, 4795-4804. http://dx.doi.org/10.1021/acsnano.2c00101

(118) Deng, X.; Yang, Y.; Wang, L.; Fu, X.-Z.; Luo, J.-L. "Metallic Co Nanoarray Catalyzes Selective NH3 Production from Electrochemical Nitrate Reduction at Current Densities Exceeding 2 A cm−2," *Advanced Science* **2021**, *8*, 2004523. http://dx.doi.org/https://doi.org/10.1002/advs.202004523

(119) Ge, Z.-X.; Wang, T.-J.; Ding, Y.; Yin, S.-B.; Li, F.-M.; Chen, P.; Chen, Y. "Interfacial Engineering Enhances the Electroactivity of Frame-Like Concave RhCu Bimetallic Nanocubes for Nitrate Reduction," *Advanced Energy Materials* **2022**, *12*, 2103916. http://dx.doi.org/https://doi.org/10.1002/aenm.202103916

(120) He, W. Z., Jian; Dieckhöfer, Stefan; Varhade, Swapnil; Brix, Ann Cathrin; Lielpetere, Anna; Seisel, Sabine; Junqueira, João R C; Schuhmann, Wolfgang "Splicing the active phases of copper/cobalt-based catalysts achieves high-rate tandem electroreduction of nitrate to ammonia," *Nature Communications* **2022**, *13*, 1129. http://dx.doi.org/10.1038/s41467-022-28728-4

(121) Fang, Z.; Jin, Z.; Tang, S.; Li, P.; Wu, P.; Yu, G. "Porous Two-dimensional Iron-Cyano Nanosheets for High-rate Electrochemical Nitrate Reduction," *ACS Nano* **2022**, *16*, 1072-1081. http://dx.doi.org/10.1021/acsnano.1c08814

(122) Fan, X.; Xie, L.; Liang, J.; Ren, Y.; Zhang, L.; Yue, L.; Li, T.; Luo, Y.; Li, N.; Tang, B.; Liu, Y.; Gao, S.; Alshehri, A. A.; Liu, Q.; Kong, Q.; Sun, X. "In situ grown Fe3O4 particle on stainless steel: A highly efficient electrocatalyst for nitrate reduction to ammonia," *Nano Research* **2022**, *15*, 3050-3055. http://dx.doi.org/10.1007/s12274-021-3951-5

(123) Deng, Z.; Liang, J.; Liu, Q.; Ma, C.; Xie, L.; Yue, L.; Ren, Y.; Li, T.; Luo, Y.; Li, N.; Tang, B.; Ali Alshehri, A.; Shakir, I.; Agboola, P. O.; Yan, S.; Zheng, B.; Du, J.; Kong, Q.; Sun, X. "High-efficiency ammonia electrosynthesis on self-supported Co2AlO4 nanoarray in neutral media by selective reduction of nitrate," *Chemical Engineering Journal* **2022**, *435*, 135104. http://dx.doi.org/https://doi.org/10.1016/j.cej.2022.135104

(124) Wei, P.; Liang, J.; Liu, Q.; Xie, L.; Tong, X.; Ren, Y.; Li, T.; Luo, Y.; Li, N.; Tang, B.; Asiri, A. M.; Hamdy, M. S.; Kong, Q.; Wang, Z.; Sun, X. "Iron-doped cobalt oxide nanoarray for efficient electrocatalytic nitrate-to-ammonia conversion," *Journal of Colloid and Interface Science* **2022**, *615*, 636-642. http://dx.doi.org/https://doi.org/10.1016/j.jcis.2022.01.186

(125) Liu, Q.; Xie, L.; Liang, J.; Ren, Y.; Wang, Y.; Zhang, L.; Yue, L.; Li, T.; Luo, Y.; Li, N.; Tang, B.; Liu, Y.; Gao, S.; Alshehri, A. A.; Shakir, I.; Agboola, P. O.; Kong, Q.; Wang, Q.; Ma, D.; Sun, X. "Ambient Ammonia Synthesis via Electrochemical Reduction of Nitrate Enabled by NiCo2O4 Nanowire Array," *Small* **2022**, *18*, 2106961. http://dx.doi.org/https://doi.org/10.1002/smll.202106961

(126) Chen, Q.; Liang, J.; Yue, L.; Luo, Y.; Liu, Q.; Li, N.; Alshehri, A. A.; Li, T.; Guo, H.; Sun, X. "CoO nanoparticle decorated N-doped carbon nanotubes: a high-efficiency catalyst for nitrate reduction to ammonia," *Chemical Communications* **2022**, *58*, 5901-5904. http://dx.doi.org/10.1039/D2CC00997H

(127) Harmon, N. J.; Rooney, C. L.; Tao, Z.; Shang, B.; Raychaudhuri, N.; Choi, C.; Li, H.; Wang, H. "Intrinsic Catalytic Activity of Carbon Nanotubes for Electrochemical Nitrate Reduction," *ACS Catalysis* **2022**, *12*, 9135-9142. http://dx.doi.org/10.1021/acscatal.2c01144

(128) Wang, J.; Wu, D.; Li, M.; Wei, X.; Yang, X.; Shao, M.; Gu, M. "Bismuth Ferrite as an Electrocatalyst for the Electrochemical Nitrate Reduction," *Nano Letters* **2022**, *22*, 5600-5606. http://dx.doi.org/10.1021/acs.nanolett.2c02026

(129) Xie, M.; Tang, S.; Li, Z.; Wang, M.; Jin, Z.; Li, P.; Zhan, X.; Zhou, H.; Yu, G. "Intermetallic Single-Atom Alloy In–Pd Bimetallene for Neutral Electrosynthesis of Ammonia from Nitrate," *Journal of the American Chemical Society* **2023**, *145*, 13957-13967. http://dx.doi.org/10.1021/jacs.3c03432

(130) Chu, K.; Zong, W.; Xue, G.; Guo, H.; Qin, J.; Zhu, H.; Zhang, N.; Tian, Z.; Dong, H.; Miao, Y.-E.; Roeffaers, M. B. J.; Hofkens, J.; Lai, F.; Liu, T. "Cation Substitution Strategy for Developing Perovskite Oxide with Rich Oxygen Vacancy-Mediated Charge Redistribution Enables Highly Efficient Nitrate Electroreduction to Ammonia," *Journal of the American Chemical Society* **2023**, *145*, 21387-21396. http://dx.doi.org/10.1021/jacs.3c06402

(131) Sun, F.; Gao, Y.; Li, M.; Wen, Y.; Fang, Y.; Meyer, T. J.; Shan, B. "Molecular Self-Assembly in Conductive Covalent Networks for Selective Nitrate Electroreduction to Ammonia," *Journal of the American Chemical Society* **2023**, *145*, 21491-21501. http://dx.doi.org/10.1021/jacs.3c07320

(132) Wang, W.; Chen, J.; Tse, E. C. M. "Synergy between Cu and Co in a Layered Double Hydroxide Enables Close to 100% Nitrate-to-Ammonia Selectivity," *Journal of the American Chemical Society* **2023**, *145*, 26678-26687. http://dx.doi.org/10.1021/jacs.3c08084

(133) Hu, Q.; Yang, K.; Peng, O.; Li, M.; Ma, L.; Huang, S.; Du, Y.; Xu, Z.-X.; Wang, Q.; Chen, Z.; Yang, M.; Loh, K. P. "Ammonia Electrosynthesis from Nitrate Using a Ruthenium–Copper Cocatalyst System: A Full Concentration Range Study," *Journal of the American Chemical Society* **2024**, *146*, 668-676. http://dx.doi.org/10.1021/jacs.3c10516

(134) Hu, Q.; Qi, S.; Huo, Q.; Zhao, Y.; Sun, J.; Chen, X.; Lv, M.; Zhou, W.; Feng, C.; Chai, X.; Yang, H.; He, C. "Designing Efficient Nitrate Reduction Electrocatalysts by Identifying and Optimizing Active Sites of Co-Based Spinels," *Journal of the American Chemical Society* **2023**. http://dx.doi.org/10.1021/jacs.3c06904

(135) Liu, Q.; Liu, Q.; Xie, L.; Ji, Y.; Li, T.; Zhang, B.; Li, N.; Tang, B.; Liu, Y.; Gao, S.; Luo, Y.; Yu, L.; Kong, Q.; Sun, X. "High-Performance Electrochemical Nitrate Reduction to Ammonia under Ambient Conditions Using a FeOOH Nanorod Catalyst," *ACS Applied Materials & Interfaces* **2022**, *14*, 17312-17318. http://dx.doi.org/10.1021/acsami.2c00436

(136) Jiang, M.; Su, J.; Song, X.; Zhang, P.; Zhu, M.; Qin, L.; Tie, Z.; Zuo, J.-L.; Jin, Z. "Interfacial Reduction Nucleation of Noble Metal Nanodots on Redox-Active Metal–Organic

Frameworks for High-Efficiency Electrocatalytic Conversion of Nitrate to Ammonia," *Nano Letters* **2022**, *22*, 2529-2537. http://dx.doi.org/10.1021/acs.nanolett.2c00446

(137) Liu, H.; Timoshenko, J.; Bai, L.; Li, Q.; Rüscher, M.; Sun, C.; Roldan Cuenya, B.; Luo, J. "Low-Coordination Rhodium Catalysts for an Efficient Electrochemical Nitrate Reduction to Ammonia," *ACS Catalysis* **2023**, *13*, 1513-1521. http://dx.doi.org/10.1021/acscatal.2c03004

(138) Wu, K.; Sun, C.; Wang, Z.; Song, Q.; Bai, X.; Yu, X.; Li, Q.; Wang, Z.; Zhang, H.; Zhang, J.; Tong, X.; Liang, Y.; Khosla, A.; Zhao, Z. "Surface Reconstruction on Uniform Cu Nanodisks Boosted Electrochemical Nitrate Reduction to Ammonia," *ACS Materials Letters* **2022**, *4*, 650-656. http://dx.doi.org/10.1021/acsmaterialslett.2c00149

(139) Lim, J.; Liu, C.-Y.; Park, J.; Liu, Y.-H.; Senftle, T. P.; Lee, S. W.; Hatzell, M. C. "Structure Sensitivity of Pd Facets for Enhanced Electrochemical Nitrate Reduction to Ammonia," *ACS Catalysis* **2021**, *11*, 7568-7577. http://dx.doi.org/10.1021/acscatal.1c01413

(140) Deng, Z.; Ma, C.; Fan, X.; Li, Z.; Luo, Y.; Sun, S.; Zheng, D.; Liu, Q.; Du, J.; Lu, Q.; Zheng, B.; Sun, X. "Construction of CoP/TiO2 nanoarray for enhanced electrochemical nitrate reduction to ammonia," *Materials Today Physics* **2022**, *28*, 100854. http://dx.doi.org/https://doi.org/10.1016/j.mtphys.2022.100854

(141) Luo, Y.; Chen, K.; Shen, P.; Li, X.; Li, X.; Li, Y.; Chu, K. "B-doped MoS2 for nitrate electroreduction to ammonia," *Journal of Colloid and Interface Science* **2023**, *629*, 950-957. http://dx.doi.org/https://doi.org/10.1016/j.jcis.2022.09.049

(142) Liu, H.; Lang, X.; Zhu, C.; Timoshenko, J.; Rüscher, M.; Bai, L.; Guijarro, N.; Yin, H.; Peng, Y.; Li, J.; Liu, Z.; Wang, W.; Cuenya, B. R.; Luo, J. "Efficient Electrochemical Nitrate Reduction to Ammonia with Copper-Supported Rhodium Cluster and Single-Atom Catalysts," *Angewandte Chemie International Edition* **2022**, *61*, e202202556. http://dx.doi.org/https://doi.org/10.1002/anie.202202556

(143) Fan, K.; Xie, W.; Li, J.; Sun, Y.; Xu, P.; Tang, Y.; Li, Z.; Shao, M. "Active hydrogen boosts electrochemical nitrate reduction to ammonia," *Nature Communications* **2022**, *13*, 7958. http://dx.doi.org/10.1038/s41467-022-35664-w

(144) Wang, G.; Shen, P.; Chen, K.; Guo, Y.; Zhao, X.; Chu, K. "Rare-earth La-doped VS2−x for electrochemical nitrate reduction to ammonia," *Inorganic Chemistry Frontiers* **2023**, *10*, 2014-2021. http://dx.doi.org/10.1039/D2QI02757G

(145) Zhou, Y.; Duan, R.; Li, H.; Zhao, M.; Ding, C.; Li, C. "Boosting Electrocatalytic Nitrate Reduction to Ammonia via Promoting Water Dissociation," *ACS Catalysis* **2023**, *13*, 10846-10854. http://dx.doi.org/10.1021/acscatal.3c02951

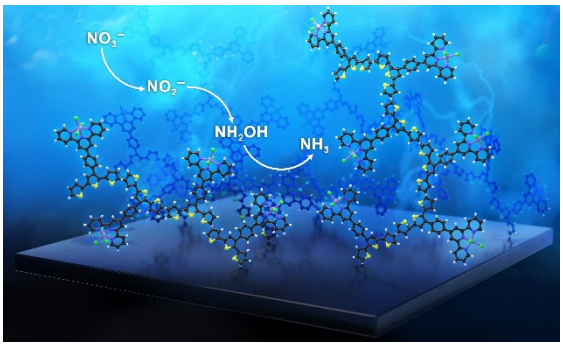

For Table of Contents Only